Advanced Time Imaging

Dissertation

zur Erlangung des Doktorgrades der Naturwissenschaften

an der Fakultät für Mathematik, Informatik und Naturwissenschaften

Fachbereich Geowissenschaften

der Universität Hamburg

vorgelegt von Martina Glöckner

aus Frankfurt (Oder), Deutschland

Hamburg, 2019

Als Dissertation angenommen am Fachbereich Geowissenschaften

Tag des Vollzugs der Promotion:	11.12.2019
Gutachter/Gutachterinnen:	Prof. Dr. Dirk Gajewski PD Dr. Claudia Vanelle
Vorsitzender des Fachpromotionsausschusses Geowissenschaften:	Prof. Dr. Dirk Gajewski

Abstract

Time imaging methods are important and widely used in industry and academia. A first guess of a subsurface image can be achieved quickly with time migration. There are several different techniques which aim to improve the migration result. In this work, I consider two techniques in more detail, migration denoising and migration velocity analysis (MVA). I introduce a loop of migration and the inverse process, demigration. These methods are based on the implicit common-reflection surface (CRS) operator and provide the basis for the denoising and MVA. The reduction of the noise content in seismic data has been performed for a long a time. I investigate three different methods, which partly build on each other, to increase the signal-to-noise ratio (SNR) of the data. The application of the migration/demigration loop leads to a first noise reduction. This process is used as input for the migration deconvolution and the deep convolutional neuronal network. All methods suppress different kinds of noise in the data. The introduced MVA is a two step process. First a velocity model is automatically calculated using the kinematic wavefield attributes, which are available after a multi-parameter stack. The second step includes the MVA with a refinement of the velocities. I suggest using the coherence section of the migrated image as a mask to identify prominent reflections and weaker diffractions with higher coherence values. These areas are linked by a subsequent interpolation and smoothing. All presented methods are applied to a field data set including salt diapirs and complex subsurface structures. The denoising methods and the MVA significantly improve the migrated image, especially in the salt area and nearby regions. In addition, some techniques are extended to 3D to process challenging 3D P-cable data. The characteristic of this special kind of acquisition are short source-receiver offsets and a high frequency source. This leads to an increased resolution and makes conventional velocity-model building practically impossible without additional information. I suggest a method based on diffraction processing to obtain velocities suitable for time migration. Diffractions are energy that was scattered in all directions by small-scale objects. This property can be used as a tool for the suggested velocity-model building even for short, source-receiver offsets. This procedure is the first consistent approach that leads to a 3D time-migrated image of P-cable data.

Zusammenfassung

Bildgebende Verfahren im Zeitbereich sind wichtig und finden häufig Anwendung in der Industrie und im akademischen Bereich. Ein erstes Untergrundbild im Zeitbereich kann schnell mit einer Zeitmigration erzeugt werden. Es gibt verschiedene Techniken, die dieses Bild verbessern können. In dieser Arbeit präsentiere ich zwei dieser Techniken. Diese sind das Entrauschen von Bildern und die Migrationsgeschwindigkeitsanalyse. Dafür entwickle ich eine Schleife aus Migration und der inversen Methode, der Demigration. Diese Operatoren basieren auf der Methode der implizierten gemeinsamen Reflektionsfläche und bilden die Basis für das Entrauschen und die Migrationsgeschwindigkeitsanalyse. Die Reduzierung des Rauschens in seismischen Daten ist schon lange ein Part der allgemein durchgeführten Arbeitsschritte. Ich untersuche drei Methoden zur Verbesserung des Signal zu Rauschen Verhältnisses in den Daten, die teilweise aufeinander aufbauen. Die Anwendung der Schleife aus Migration und Demigration führt zu einer ersten Verbesserung des Verhältnisses. Diese Schleife dient als Eingangsgröße für die Migrationdekonvolution und für das tiefe neuronale Konvolutionsnetzwerk. Alle Methoden unterdrücken verschiedene Arten von Störsignalen. Die vorgestellte Migrationsgeschwindigkeitsanalyse ist ein zweistufiger Prozess. Zuerst wird ein Geschwindigkeitsmodell aus den kinematischen Wellenfeldattributen berechnet. Diese stehen nach einer Multiparameterstapelung zur Verfügung. Der zweite Schritt beinhaltet die Migrationsgeschwindigkeitsanalyse mit einer Verfeinerung der Geschwindigkeiten. Dafür wird die Kohärenzsektion des migrierten Bildes als Filter verwendet um prominente Reflektionen und schwache Diffraktionen mit höheren Kohärenzwerten zu identifizieren. Diese Bereiche werden durch eine Interpolation und Glättung miteinander verbunden. Alle präsentierten Methoden zur Verbesserung des Signal zu Rauschen Verhältnisses und die Migrationsgeschwindigkeitsanalyse werden auf Felddaten mit Salzdiapiren und komplexen Untergrundstrukturen angewendet. Sie verbessern das migrierte Bild deutlich in Bereichen mit Salz und umliegenden Strukturen. Zusätzlich werden einige dieser Methoden auf drei Dimensionen erweitert um anspruchsvolle 3D P-cable Daten zu prozessieren. Die Merkmale dieser speziellen Akquisitionstechnik sind kurze Quell- und Empfängerabstände und eine hochfrequente Quelle. Dies führt zu einer Verbesserung der Auflösung und macht konventionelle Migrationsgeschwindigkeitsanalyse ohne Zusatzinformationen fast unmöglich. Ich schlage eine Methode vor, die auf dem Prozessieren von Diffraktionen beruht, um Geschwindigkeiten für eine Zeitmigration zu erhalten. Diffraktionen setzen sich aus Energie, die von kleinskaligen Objekte in alle Richtungen gestreut wurde, zusammen. Diese Eigenschaft wird zur Berechnung eines Geschwindigkeitsmodells auch mit kurzen Quell- und Empfängerabständen genutzt. Dieser Prozess ist die erste konsistente Vorgehensweise um 3D zeitmigrierte Bilder von P-cable Daten zu erhalten.

Contents

List of Figures

1 Introduction

In the 20th century reflection seismologists started to image the earth's interior. First companies (for example, Geological Engineering Company and Seismos) were founded with the aim of salt body detection, finding petroleum and mining objectives (Sheriff and Geldart, 1995). Until the 1960s processing of the recorded seismic data was a manual process without the use of advanced techniques in daily data analysis (Claerbout et al., 1996). Claerbout (1970) introduced an imaging method based on the wave equation and replaced the ad hoc fashion of image making. The oil and gas industry supported this development and it became the leading processing technique. Processing improved fast. Claerbout et al. (1996) formulates the aim of that time as follows: the main goal 'is to make good pictures of the earth's interior from the' measured data. A simplified seismic experiment is shown in Figure 1.1. It displays how data is measured on the surface. Innumerable new processing techniques have been invented and existing techniques have been improved by means of computers. Techniques that are important for this work are presented in the following paragraphs.

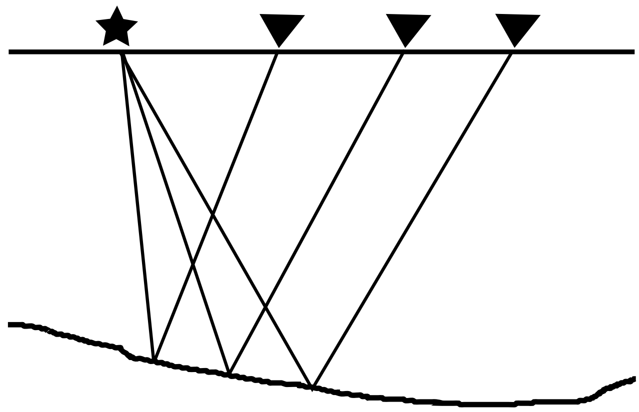

Figure 1.1: Simplified sketch of a seismic experiment. The star denotes a seismic source and the triangles the receivers. Source and receivers are located at the surface and measure the reflected energy from subsurface structures. Numerous sources and receivers yield the seismic data. The individual distance between one source and one receiver is called offset and is important for illumination aspects and velocity determination.

1.1 Migration

Migration is a process of subsurface imaging and is needed because the recorded data does not mirror the true subsurface. It has the aim to correct seismic data for geological features such as faults, inclined horizons, flanks, and diffractions (e.g. Sheriff and Geldart, 1995). Furthermore, it adjusts object distortions, e.g., adapts length, dip, and curvature of reflections, and collapses diffractions (see Figure 1.2). Migration can be divided into depth and time migration, although here only time migration is under consideration. The advantages of time migration are: it does not require explicit modeling, it is less sensitive to model errors than depth migration, it improves the signal-to-noise ratio (SNR) and resolution in comparison with stacking. The disadvantages are that time migration is not designed to handle complex laterally varying structures (Yilmaz, 2001), and that it suffers from imperfections from, e.g., the used operator, exhibiting artifacts (Hertweck et al., 2003), uneven illumination, imperfect acquisition, finite-recording aperture. There are some underlying assumptions for time migration: the straight ray propagation, regularly sampled data, and infinite migration aperture. Sufficiently complex data violate these assumptions. Nevertheless, time migration is a widely used tool in industry and academia to get a first insight into the data because of the fast and robust processing.

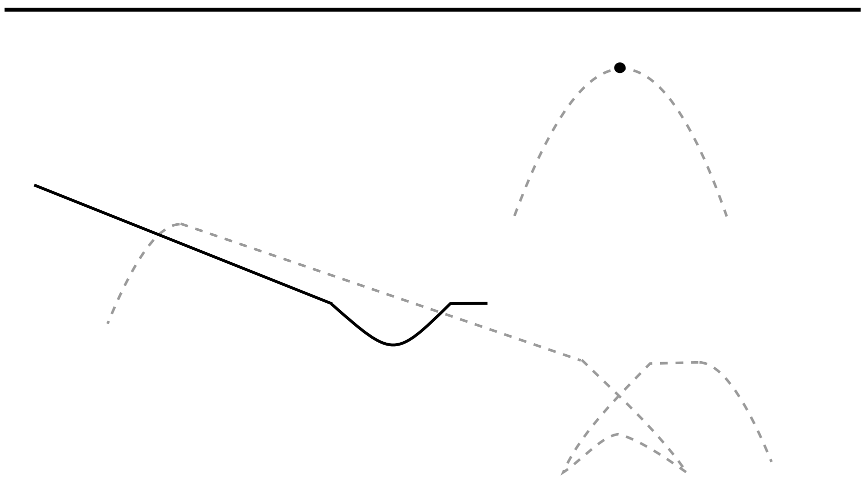

Figure 1.2: Sketch of migration principle. The dashed grey lines show the unmigrated events. The solid black lines show the migrated events. The hyperbola collapses to a diffraction point at its apex. The dipped reflection is shortened and moved up dip after migration. The triplication (x-shaped event) is unfolded into a syncline. The two unilateral hyperbolae at the end points of the reflection are collapsed.

Huygens (1690) describes wave propagation as a process where the wavefront is considered as the sum of spherical wavelets. Furthermore, he states that every point serves as a source of spherical wavelets. Hagedoorn (1954) applies Huygens principle to geophysics and introduces the first migration method, so-called 'string construction' or 'ruler-and-compass method'. Schneider (1978) explains basic migration principles and shows an integral formulation for migration. Another method is the diffraction summation (see Yilmaz, 2001). Diffractors are small-scale objects, smaller than a quarter of the wavelength, and serve as Huygens secondary sources. The data is summed along the diffraction hyperbola for every subsurface point. Kirchhoff migration (e.g. Yilmaz, 2001) adds different factors to the principle of the diffraction summation. These factors are: the obliquity, spherical spreading, and a wavelet shaping factor to account for the amplitude and phase of the data (dynamic consideration).

I present a time-migration approach similar to the Kirchhoff migration. The approach is based on a multiparameter operator, the so-called implicit common-reflection surface (Schwarz et al., 2014) and uses an apex-based operator for time migration. Here, we consider kinematic aspects and only use the wavelet shaping factor to partly account for amplitudes. Furthermore, all migration methods have in common that they require an appropriate starting velocity model. Migration is often applied iteratively with the goal of an improved velocity model to obtain a final result. This procedure is called migration velocity analysis (MVA) and is the topic of the next section. A second feature of migration is the SNR improvement or denoising ability, which will be investigated, too.

1.2 Migration velocity analysis

The migration velocity model is an important feature because it determines the quality of the migrated image. The velocity should be appropriate, smooth, and consistent with the data. The velocity model can serve as a starting model for wavefront-based inversion methods, e.g. full-waveform inversion, to obtain a subsurface image in depth. In general, one can observe that the horizontal displacement of events is proportional to the square of the migration velocity, and proportional to dips (Yilmaz, 2001). Migration with inappropriate velocity models leads to artifacts, such as misplaced events, frowns (overestimated velocities), and smiles (underestimated velocities) (e.g. Zhu et al., 1998). These artifacts are tackled by MVA to improve the migrated image. Figure 1.3 illustrates the effect (smiles and frowns) of an incorrect migration velocity.

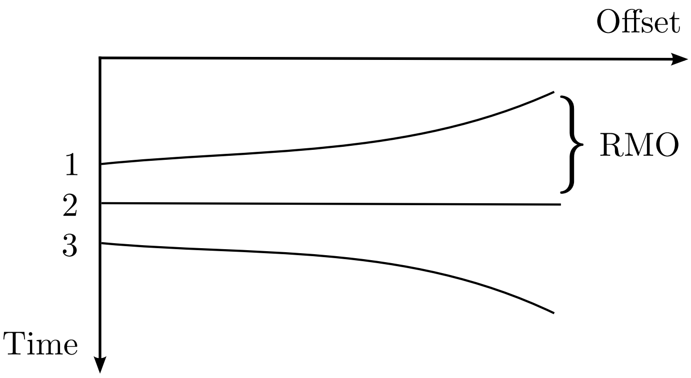

Figure 1.3: Sketch of a migration velocity analysis with a so-called common-image gather in time and residual moveout analysis. A flat line (2) indicates an appropriate migration velocity. A lower velocity (1) in comparison with case (2) leads to a smile. A higher velocity (3) results in a frown. The discrepancy at the end to a flat line is the residual moveout (RMO) and can be used as a correction term in an iterative analysis.

The first step is always to determine a starting-velocity model and account for velocity errors with a MVA. Different techniques can be applied. A simple method is a constant-velocity scan (for example Yilmaz, 2001), where different velocities are tested. This is followed by a picking of flat events, which means an appropriate velocity for the event under consideration. Residual moveout (RMO) analysis of common-image gathers (CIG) is another technique to account for velocity errors. Data is sorted to a common-midpoint (CMP) and the flatness of events along the offset is investigated and corrected for with a lower or higher velocity for the event under consideration (e.g. Yilmaz, 2001). Another technique is introduced by Gardner et al. (1974) and compares different common-offset images to improve the velocity model. Shurtleff (1984) introduces a constant-velocity migration in the frequency - wavenumber (f-k) domain. A focusing analysis, introduced by Yilmaz and Chambers (1984), uses a double-square-root (DSR) operator in the Fourier transform domain. The velocity-independent prestack migration (Fowler, 1985) relates dip-dependent stacking velocities with dip-independent dip-moveout corrected (DMO) velocities, followed by picking and interpolation to obtain a velocity model. Yilmaz (2001) describes a common-offset migration of DMO corrected gathers. The equivalent offset migration (Bancroft et al., 1998) focuses common-scatterpoint (CSP) gathers with a simplified Kirchhoff migration. Fomel (2003) uses velocity continuation in CIG in combination with iterative RMO. Based on this method, Schleicher et al. (2008) presents the image-wave propagation with an enhanced RMO correction taking vertical and lateral movements into account. Another MVA technique is the migration of common-reflection-point (CRP) gather before the stack, followed by the analysis of flat events (Yilmaz, 2001). Dell et al. (2012) introduces the common-migrated-reflector-element stack of CSP gather with an automatic velocity update. Another method, presented by Spinner (2007), uses kinematic wavefield attributes (Hubral, 1983) to calculate velocities and perform a Kirchhoff-like migration.

I use kinematic wavefield attributes, which are determined automatically from the implicit CRS operator (Schwarz, 2011), to calculate a time-migration-velocity model. In contrast to other presented methods in the preceding paragraph, no prior velocity information is necessary. I derive a Kirchhoff-like time-migration operator based on the implicit CRS operator. Furthermore, I present a MVA technique based on a coherence weighting. Coherence describes local similarity of wavefronts along the data trace. Values are large in areas with appropriate migration velocities and serve as a filter. These areas are linked with interpolation to obtain an improved migrated image. This refinement also reduces migration noise.

1.3 Migration denoising

Noise is a part of seismic data. Generally, noise can be divided in two parts: random and coherent noise (Yilmaz, 2001). Random noise includes temporal direction and spatially uncorrelated noise. Coherent noise covers reverberations, multiples, and linear noise, e.g., guided waves, ground roll, and swell noise. Figure 1.4 shows an example for denoising by stacking. Here, an additional regularization of traces is also included and leads to an improved and denoised image.

A lot of different techniques have been invented to denoise data. Treitel (1974) uses the Wiener filter for deconvolution, which is a process of wavelet shortening. Canales (1984) introduces spatial prediction filtering in the form of a spiking deconvolution operator to account for noise. There are some standard techniques to increase the signal-to-noise ratio overall, namely f-k filtering, τ-p transform, or Radon transform techniques (for example Yilmaz, 2001). Furthermore, more advanced techniques exist, e.g. non-local-means filter

(Bonar and Sacchi, 2012), and dictionary learning (Beckouche and Ma, 2014). In addition, techniques from other image denoising disciplines, e.g. medical imaging, can be applied to seismic data. Often machine learning (ML) algorithms are used to denoise images (e.g. Goodfellow et al., 2016). Vincent et al. (2010) uses ML to denoise natural scene images and hand-written numbers. Agostinelli et al. (2013) applies ML algorithms in medical image denoising. These techniques can be adapted for denoising seismic images.

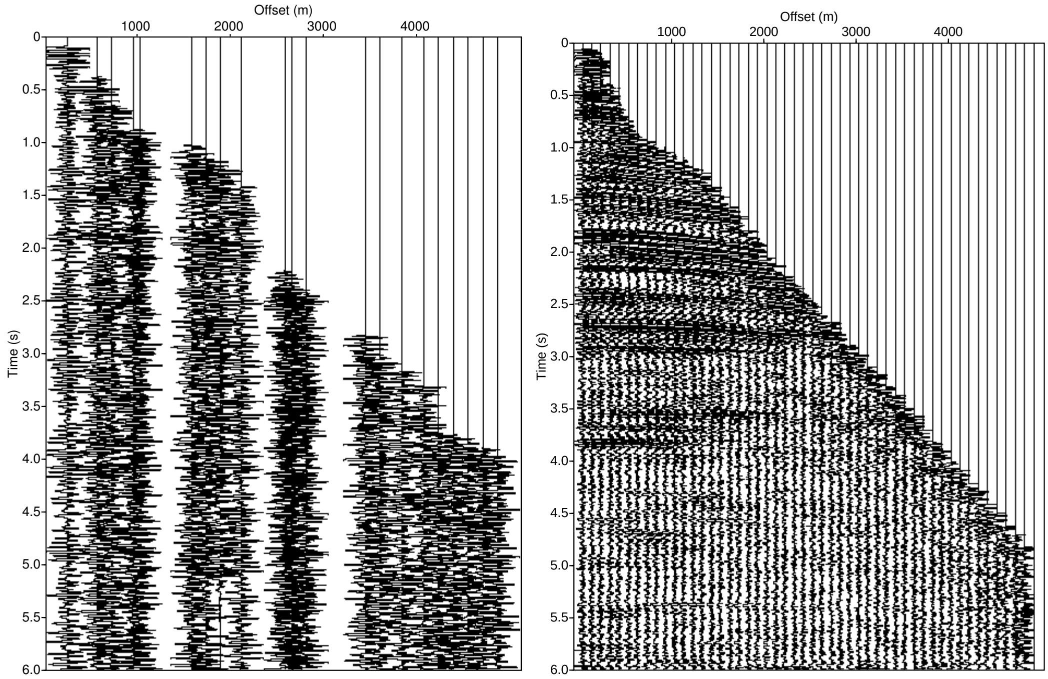

(a) Original data.
(b) Denoised data.

Figure 1.4: Example for denoising data with the so-called partial stack (Baykulov and Gajewski, 2009). This special technique is able to improve the SNR and fill acquisition gaps. The example shows the original data a) from a land data set with gaps due to ,e.g. streets, missing permissions, erroneous channels. The denoised data b) are regularized and events are visible. The land data example is the same as later used in chapters 2 and 3.

I investigate three denoising methods with the aim to improve the migrated image. The first denoising approach makes use of the duality of modeling and imaging operators (Hubral et al., 1996; Tygel et al., 1996). I introduce a migration/demigration method based on the implicit CRS operator to denoise the data. The application of demigration itself leads to noise reduction, which mainly manifests in a smoother image under the assumption of an appropriate velocity model. Another investigated denoising method is the migration deconvolution. The operator duality of migration and demigration (Claerbout et al., 1996) allows a least-squares formulation for the migration. Therefore, an inverse, so-called deconvolution operator (Hu et al., 2001), has to be approximated to correct for amplitudes and improve the SNR. The result is a decrease of the noise content in the migrated image. The last denoising technique presented here is based on a ML algorithm, a supervised autoencoder. I use a deep convolutional neuronal network to denoise the migrated image. The trained network is applied to the migrated image to obtain a denoised image. The advantage of such networks is that no assumptions are made concerning the medium or operator. For example, the CRS operator is hyperbolic and leads to inaccuracies for strong lateral varying structures, and heterogeneous mediums.

1.4 Structure of the thesis

The first paper 'Velocity-estimation improvements and migration/demigration using the common-reflection surface with continuing deconvolution in the time domain' by Glöckner et al. (2019a) presented in Chapter 2 includes all aspects of migration, MVA, and denoising without ML explained in the introduction. The automatic velocity-model building with the subsequent refinement (MVA) is explained. Two of the mentioned denoising methods follow, namely denoising by demigration and based on this, the migration deconvolution. The denoising techniques are applied to synthetic and field data to investigate their denoising ability.

Chapter 3 contains the paper 'Denoising migrated data with a deep neuronal network' by Glöckner et al. (2019b). The third denoising method, the supervised autoencoder, is presented here. The method is applied to field data and the denoising ability is described. Furthermore, this paper investigates data augmentation. It can be used in the case of too little usable data and increase the amount of meaningful data by , e.g. rotation, flipping, contrast and saturation changes.

Chapter 4 shows the application and extension of some presented techniques to challenging 3D P-cable data and the paper is titled 'Imaging zero-offset 3D P-cable data with CRS method' by Glöckner et al. (2019c). This special marine acquisition system includes a high-frequency source and short cable lengths (offset). The comparably cheap 3D acquisition leads to an improved resolution and is mostly used in academia. The calculation of the velocity model is not possible with conventional approaches. I present a diffraction-based work flow for a 3D multi-parameter stack, utilizing the kinematic wavefield attributes for a highly automated subsequent velocity-model refinement (MVA). 3D time migration results are presented for this special kind of data.

The conclusions are drawn in Chapter 5. The outlook, Chapter 6, contains more research about my work with the P-cable data and presents possible future work.

1.5 Contribution of Co-authors

In the following, I point out the contributions of my co-authors for each paper separately in the order they are presented in this work.

Sergius Dell provided the migration deconvolution. He, as well as Benjamin Schwarz, Claudia Vanelle and Dirk Gajewski, contributed with proof-reading and helpful discussions on the general structure. The velocity calculation and refinement, as well as migration and demigration with the data application were performed by myself.

Jan Walda provided the neuronal network framework. Sergius Dell and Dirk Gajewski gave strategic hints for publication. Training, data augmentation, and data application were performed by myself.

Jan Walda provided the 3D code for stacking and further contributed with continuous discussion. Sergius Dell performed the 3D time migration. Dirk Gajewski gave valuable hints and discussion contributions. The colleagues from the GEOMAR, Dirk Kläschen, Jens Karstens and Christian Berndt provided the 3D P-cable data and did the preprocessing. They answered all questions concerning the data acquisition. The further development and application of the 3D code, as well as, the migration velocity analysis in 3D were performed by myself.

2 Velocity-estimation improvements and migration/demigration using the common-reflection surface with continuing deconvolution in the time domain

2.1 Abstract

To obtain an image of the earth's subsurface, time-imaging methods can be applied, as they are reasonably fast, less sensitive to velocity model errors than depth-imaging methods and, usually, easy to parallelize. A powerful tool for time-imaging consists of a series of prestack time-migrations and demigrations. We apply multi-parameter stacking techniques to obtain an initial time-migration velocity model. The velocity model building proposed here is based on the kinematic wavefield attributes of the common-reflection surface method. A subsequent refinement of the velocities uses a coherence filter which is based on a predetermined threshold, and followed by an interpolation and smoothing. Then, we perform a migration deconvolution to obtain the final time-migrated image. The migration deconvolution consists of one iteration of least-squares migration with an estimated Hessian. We estimate the Hessian by non-stationary matching filters, i.e., in a data-driven fashion. The model building uses the framework of the common-reflection-surface , and the migration deconvolution is fully automated. Therefore, minimal user interaction is required to carry out both the velocity model refinement and the image update. We apply the suggested approaches of velocity refinement and migration deconvolution to complex synthetic and field data.

2.2 Introduction

Time migration is an attractive tool to produce subsurface images because it is reasonably fast, less sensitive to the model errors than depth migration and, usually, a massively parallelized technique. A highly focused time image is, however, achievable only with sufficiently well-determined migration velocities. Thus, a refinement of the initial time-migration velocities is often applied to obtain an improved final image. Also, time migration is derived by considering many assumptions, among others a straight ray propagation, regularly sampled seismic data and an infinite migration aperture. However, these assumptions are violated when sufficiently complex subsurface structures and field data are considered. Thus, time-migrated images usually suffer from imperfections of the operator, exhibiting artifacts (Hertweck et al., 2003), such as the commonly observed migration swings. Conventionally, a residual moveout (RMO) analysis is used to reduce the impact of the model errors on the image, (e.g., Yilmaz (2001)). The RMO analysis is an iterative approach to update velocities based on the analysis of the flattening of events in the common-image gathers (CIG) after time migration. Another approach to perform the velocity update after prestack time-migration is common-offset migration followed by application of inverse normal moveout (NMO) and subsequent velocity analysis on the newly generated gathers. The obtained gathers contain time-migrated reflections with approximately hyperbolic moveout and are therefore suitable for classical one-dimensional or multi-dimensional velocity analysis Dell et al. (2012). To reduce migration artifacts, several image-enhancement techniques, e.g., dip- or structure-oriented filters, are usually applied after time migration. These methods, however, can introduce a certain smoothing into the migrated images, which may increase uncertainties in fault interpretation.

A comprehensive imaging theory based on migration and demigration in the depth domain is presented by Hubral et al. (1996) and Tygel et al. (1996). In their work, Huygens surfaces and isochrons form the central ingredients, and are combined with proper amplitude weighting to preserve amplitudes. Similar to the works mentioned above, Iversen et al. (2012) presented a time-based approach. They used reflection times, slopes, and curvatures as parameters to perform migration and demigration. Here, we propose a technique to solve both time-migration problems mentioned earlier, i.e., migration artifacts and velocity analysis. Our method is based on the duality of modeling/imaging operators (see Claerbout et al., 1996). For one thing, time migration can be achieved by summation over traces (amplitude stacking) which aims to focus events, correct dips, unfold triplications, and collapse diffractions. Following Yilmaz (2001), a corresponding migration operator can be described by a double-square-root equation. While for the other thing, time demigration can be carried out by performing a semicircle superposition (amplitude spreading) which aims to restore (model) seismic data based on provided reflectivity models. The smearing (demigration) of the amplitudes can be described by a single-square-root equation. In this case, we use the same traveltimes for both steps. The advantage of the cascaded forward and backward transformation is data enhancement and regularization due to the incorporated summation of the migration, which reduces noise. Furthermore, a general conflicting dip handling is naturally incorporated in the migration process. On the one hand, a correctly migrated image should not contain conflicting dips with the exception of multiples. On the other hand, the demigration reconstructs the dips in the original unmigrated domain. A condition to perform these steps is a suitable velocity model, which can be automatically generated via, e.g., the common-reflection-surface (CRS) method (Jäger et al., 2001).

In the first part of the paper, we suggest an efficient strategy to calculate an original starting velocity model and introduce a refinement of the migration velocities. The method utilizes kinematic wavefield attributes of the CRS method, i.e., angles and curvatures of wavefronts (Hubral, 1983) and also uses a coherence filtering of the velocities, which further conditions the final velocity model for migration. In the second part, we describe the migration and demigration in terms of traveltimes. Furthermore, we briefly review the theory of least-squares migration and show that our time-migration/demigration approach can also be used for migration deconvolution. To do this, we estimate matching filters, which are convolved with the migrated image to enhance image quality. Finally, we demonstrate the applicability of the suggested fully automated workflow for complex synthetic and field-data examples.

2.3 Conceptual framework

2.3.1 Automatic velocity model building using CRS

We perform a multidimensional coherence analysis using the implicit CRS method (Vanelle et al., 2010) to extract kinematic wavefield attributes (Hubral, 1983). In principle, any double-square-root (DSR) expression (e.g., Walda et al., 2017) can be used instead of implicit CRS. An automated local coherence analysis employing the normalized semblance coefficient (Neidell and Taner, 1971) picks at every data point a subset of CRS attributes, and determines by optimization the best set consistent with the data (Nelder and Mead, 1965). The obtained kinematic wavefield attributes are described as different order terms of a Taylor series expansion of the squared hyperbolic traveltime (Müller, 1999):

$$t^2(\Delta x, \Delta h) = (t_0 + p\Delta x)^2 + 2t_0(N\Delta x^2 + M\Delta h^2) \quad . \tag{2.1a}$$

$$p = \left.\frac{\partial t}{\partial x}\right|_{x_0,h_0} \quad , \quad N = \left.\frac{\partial^2 t}{\partial x^2}\right|_{x_0,h_0} \quad , \quad M = \left.\frac{\partial^2 t}{\partial h^2}\right|_{x_0,h_0} \tag{2.1b}$$

$$p = \frac{2\sin\alpha}{v_0}, \quad , \quad M = \frac{\cos^2\alpha}{v_0 R_{NIP}} \quad , \quad N = \frac{\cos^2\alpha}{v_0 R_N} \tag{2.1c}$$

The displacement between the point under consideration (x_m, h) ,denoting midpoint and half-offset, and a central point (x_0, h_0) is $\Delta x = x_m - x_0, \Delta h = h - h_0$. The traveltime at the expansion point x_0, h_0 is denoted by t_0 and the derivatives are p, M, and N. The near-surface velocity v_0 has to be provided. An exploding-reflector experiment can be used to illustrate the physical meaning of the CRS attributes (see Figure 2.1). The angle α denotes the incidence angle of the emerging ray from a fictitious source at the normal-incident-point (NIP). R_{NIP} is the radius of curvature of the emerging wavefront at the surface from a point source at NIP. R_N is the radius of curvature of the emerging wavefront at the surface of an exploding-reflector segment around NIP.

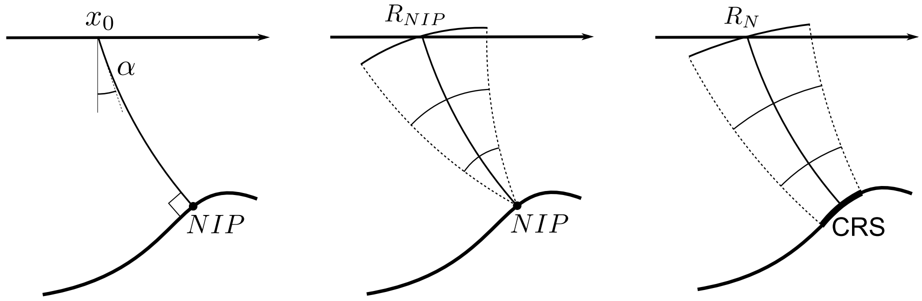

Figure 2.1: Kinematic wavefield attributes (modified after Schwarz et al. (2014)). A wave originates at the normal-incident point (NIP) and strikes the recording surface at the central zero-offset point x_0 with the emergence angle α. The radius of wavefront curvature of the NIP wave at the surface is R_{NIP}. The same applies for a wave starting at the CRS, and can be measured at the surface as radius of wavefront curvature of normal (N) wave R_N.

Then, α, R_{NIP} and R_N, extracted by local coherence analysis are used to calculate the initial (original) time-migration velocities (Schwarz et al., 2014):

$$V = \frac{v_{NMO}}{\sqrt{1 + \frac{v_{NMO}^2}{v_0^2} \sin^2 \alpha}} \quad \text{with} \quad v_{NMO} = \sqrt{\frac{2 v_0 R_{NIP}}{t_0 \cos^2 \alpha}}\,. \tag{2.2}$$

In total, the migration velocity V depends on four parameters: α, R_{NIP}, the considered time t_0, and the velocity near the surface v_0, and V is calculated for every time sample and common-midpoint. As we also consider the incidence angle α, we directly obtain dip-corrected migration velocities. Furthermore, equation 2.2 determines the normal moveout (NMO) velocity, v_{NMO}. The near-surface velocity is an important component of the migration velocity and the choice of its locally constant value is usually based on a priori information. However, the formulation of migration velocity as in equation 2.2 allows a near-surface velocity scan. This is an attractive complementary benefit of equation 2.2, particularly for data acquired in regions with very complex near-surface geology, e.g., in deserts. As a new step, we apply a coherence filter to the obtained velocity field. We perform a coherence analysis similar to the one mentioned above to obtain the semblance for the migrated image. Therefore, the semblance coefficient (equation 2.3) is calculated for every sample. It is normally described as normalized ratio of output energy to input energy (Neidell and Taner, 1971).

$$S = \frac{\sum_{i=1}^{M} \left(\sum_{j=1}^{N} A_{ij} \right)^2}{N \sum_{i=1}^{M} \sum_{j=1}^{N} A_{ij}^2}, \tag{2.3}$$

where M is the number of samples in the coherence window, N is the number of traces, and A is the amplitude of the i'th sample and j'th trace. The coefficient has values between zero (low semblance) and one (high semblance) due to the normalization. The coherence amplitude for the sample under consideration depends on the migration velocity. High coherence values mean appropriate migration velocities for this sample. In contrast to the local coherence analysis for the stacking described above, no optimization is performed, because we suppose that with the previously determined kinematic wavefield attributes an appropriate velocity is calculated. This leads to generally lower values of the migrated coherence in contrast to coherence obtained after stacking. The migrated coherence is calculated during the normal migration and is available afterwards for the velocity refinement. With the new generated attribute, we can define a threshold for the coherence that depends on the data set under consideration to eliminate noise and weak events. Only velocity values with sufficiently high semblance norm are considered for the construction of the refined velocity model. Subsequently, gaps arising from this thresholding are filled by interpolation. We use an interpolation method based on a least-squares approach, where a discrete Laplacian is used to fill the gaps. Known values are not modified with this interpolation. Afterwards, we smooth the interpolated model to obtain a smooth velocity distribution, which is necessary for time migration. As a result, areas with large coherence imply a reliable migration velocity and the subsequent interpolation connects these areas to obtain an improved migration velocity model. Furthermore, diffractions are enhanced in the suggested strategy, because they are naturally described by the used migration equation (introduced in the next subsection), whereas reflection events are merely repositioned. The migration method is designed to emphasize diffractions by summing their energy along the whole hyperbola, whereas reflections only sum over a relatively small contribution on the apex of the hyperbola. Although amplitudes of reflections are higher, coherence values of diffractions are increased a lot with this method. The procedure can be applied iteratively in such a way that the interpolated model is used again for coherence filtering, but our tests revealed that this just leads to further smoothing without improving the velocity information.

2.3.2 Migration and demigration with CRS

Generally, geophysical modeling uses linear operators that predict data from models (Claerbout et al., 1996). The inverse of modeling, inversion, aims to find models from the data and also uses linear operators. The modeling operator with respect to reflectivity is conventionally referred to as demigration. The inverse, in turn, is referred to as true-amplitude migration operator. In this paper, we formulate the time-migration and demigration based on a high-order paraxial traveltime approximation. We use implicit CRS (Schwarz et al., 2014), as it belongs to the DSR equations. As the implicit CRS method is developed to perform local coherence analysis and stacking, it is parametrized by the two-way traveltime along the central zero-offset ray . To apply it for time-migration, we rewrite the implicit CRS traveltime in terms of apex coordinates (x_{apex}, t_{apex}). These are defined by local coordinates of implicit CRS (see Appendix). We re-parametrize the diffraction subset of the implicit CRS in terms of apex coordinates:

$$t = \sqrt{\frac{t_{apex}^2}{4} + \frac{(\Delta x_a - h)^2}{V^2}} + \sqrt{\frac{t_{apex}^2}{4} + \frac{(\Delta x_a + h)^2}{V^2}}, \tag{2.4}$$

where $\Delta x_a = x_m - x_{apex}$ is the midpoint displacement, h is the half-offset, V is the time-migration velocity from equation 2.2 (Glöckner et al., 2016). This DSR expression 2.4 resembles a conventional Kirchhoff migration traveltime expression Yilmaz and Claerbout (1980) and represents the summation in our cascaded approach of migration and demigration. In equation 2.4, the traveltime t is expressed as a function of apex time t_{apex} and lateral deviation from the apex location Δx_a. To obtain the corresponding demigration expression, we find it convenient to solve equation 2.4 for t_{apex}:

$$t_{apex} = \sqrt{t^2 - \frac{4(\Delta x_a^2 + h^2)}{V^2} + \frac{16\Delta x_a^2 h^2}{t^2 V^4}}, \tag{2.5}$$

which is a single-square-root expression and represents the smearing in our cascaded approach. Both processes, migration and demigration, are likewise valid for the poststack case, where the half offset h vanishes and the equations simplify.

2.3.3 Migration deconvolution

Seismic time migration aims to map recorded data into a structural image of the earth's discontinuities. However, complex geological settings along the raypaths, uneven illumination, and imperfect acquisition with irregular surface sampling, finite recording aperture, and aliased seismic data frequently lead to seismic images which are improperly recovered by migration techniques. The migrated events appear to lose high frequencies, reveal decreased amplitudes, are erroneous in terms of shape and location, and exhibit migration swings. As a result, least-squares migration (LSM) techniques have been proposed to achieve a better matching of amplitudes in the migrated images (Schuster, 1993; Nemeth et al., 1999). The basic idea of the LSM techniques is to exploit the migration/demigration operator duality. In operator notation it reads:

$$d = Lm \,, \tag{2.6a}$$

$$m = L^{-1} d \,, \tag{2.6b}$$

where d are the seismic data, m is the reflectivity model (migration image), L is the linear modeling operator, and L^{-1} is the inverse (true-amplitude migration) operator. Usually, adjoint (transposed) instead of inverse operators are used for migration as they tolerate data imperfections and do not demand that the data provide full information (Claerbout et al., 1996).

The operator duality expressed in equation 2.6 allows us to formulate migration as a least-squares problem. If we consider the functional

$$J(m) = \frac{1}{2} \left(Lm - d \right)^2 \,, \tag{2.7}$$

we immediately see that the gradient $\nabla_m J$ yields the least-squares estimate of the reflectivity model

$$\frac{\partial J}{\partial m} = 0 \implies \hat{m} = (L'L)^{-1} L' d \,, \tag{2.8}$$

where we use the adjoint operator L' instead of the inverse operator L^{-1}. The quantity $(L'L)^{-1}$ in equation 2.8 represents the Hessian and $\hat{m}$ denotes the improved migrated image. In the literature, this inverse is frequently referred to as the resolution matrix or deconvolution operator (Hu et al., 2001), i.e., we can also use this inverse to perform a deconvolution of the migrated image $L'd$ in order to correct the amplitudes. Due to the higher-order complexity of the modeling and migration operators, the Hessian generally cannot be inverted for directly, and iterative procedures such as the conjugate gradient (CG) or the Newton method are often used (Lambaré et al., 1992). As an alternative, we use a method suggested by Guitton (2004) to approximate the effects of the Hessian with nonstationary matching filters. Apart from a convenient implementation, the method simulates the effects of least-squares inversion at a much reduced cost compared to an iterative approach. According to Guitton (2004), this strategy is set up as follows:

- Compute a first migrated image $m_1 = L'd$.
- Compute a second image $m_2 = L'Lm_1$.
- Estimate a bank of nonstationary matching filters B_0 such that $m_1 = B_0 m_2$.
- Convolve B_0 with m_1 to arrive at an improved image $\hat{m} = B_0 m_1$.

Convolution of the nonstationary matching filters with the first migrated image is equal to so-called one-iteration least-squares migration or migration deconvolution. The forward modeling (time demigration) is given by equation 2.5 and represents semi-circle superposition. The DSR migration is defined in equation 2.4 and implies hyperbolic summation. We note that the formulation of the demigration also requires a semi-circle-type superposition for migration as only this type satisfies the correctness of the adjoint migration (Ji, 1994). However, we decided to use the hyperbolic approach instead of the semicircle method because it is computationally efficient and even accounts for some potential artifacts in the image resulting from the hyperbolic summation. These artifacts usually show up for highly dipping events and are known to be caused by operator aliasing.

In the following, we investigate the applicability of the suggested strategy of automated velocity model building and migration deconvolution in the time domain using complex synthetic and field data examples.

2.4 Synthetic data example

First, we apply the presented method to the complex Sigsbee2A synthetic data. It is a constant-density acoustic data set released in 2001 by the Subsalt Multiple Attenuation Team Joint Venture (SMAART JV (Paffenholz et al., 2002)). The SMAART JV has created several 2D synthetic data sets. One of the objectives was to better understand the imaging issues contributing to the poor signal-to-noise ratio observed subsalt in deep water environments such as the Sigsbee Escarpment in the Gulf of Mexico. Prestack data were modeled with a 2D acoustic finite-difference approach with a dominant frequency of 20 Hz. The CMP spacing is 11.43 m and the offset spacing is 34.29 m. The following figures show the left part of the model containing faults and diffractor lines.

Figure 2.2 illustrates the individual steps of the velocity refinement. Figure 2.2 (a) shows the original model calculated with the CRS kinematic wavefield attributes. Its structure is dominated by laterally continuous reflections, and higher as well as lower velocities are present. Higher velocities can occur because intersecting events lead to incorrect attributes and, therefore, erroneous velocities. Figure 2.2 (b) shows the result of the coherence filtering, performed on the initial velocity estimate. We have defined a threshold for the wavefield's semblance of the time-migrated image, which depends on the data quality. The aim is to suppress noise and keep the coherence values of the events by choosing an appropriate value of the semblance coefficient. We use this as a mask for the velocity model. Here, gray corresponds to values below the threshold. Mostly reflections due to higher amplitudes in comparison to diffractions are chosen with the coherence threshold of 0.01. Figure 2.2 (c) presents the result of the interpolation of the gaps from the image in Figure 2.2 (b). Perturbations are present where gaps in the data are comparably large, especially in the right and lower part of the image due to the interpolation. Figure 2.2 (d) shows the final smoothed velocity model. Additional smoothing is necessary to fulfill the requirements for time migration. This is the reason for the decreased resolution of the refined velocity model in comparison with the original model in Figure 2.2 (a).

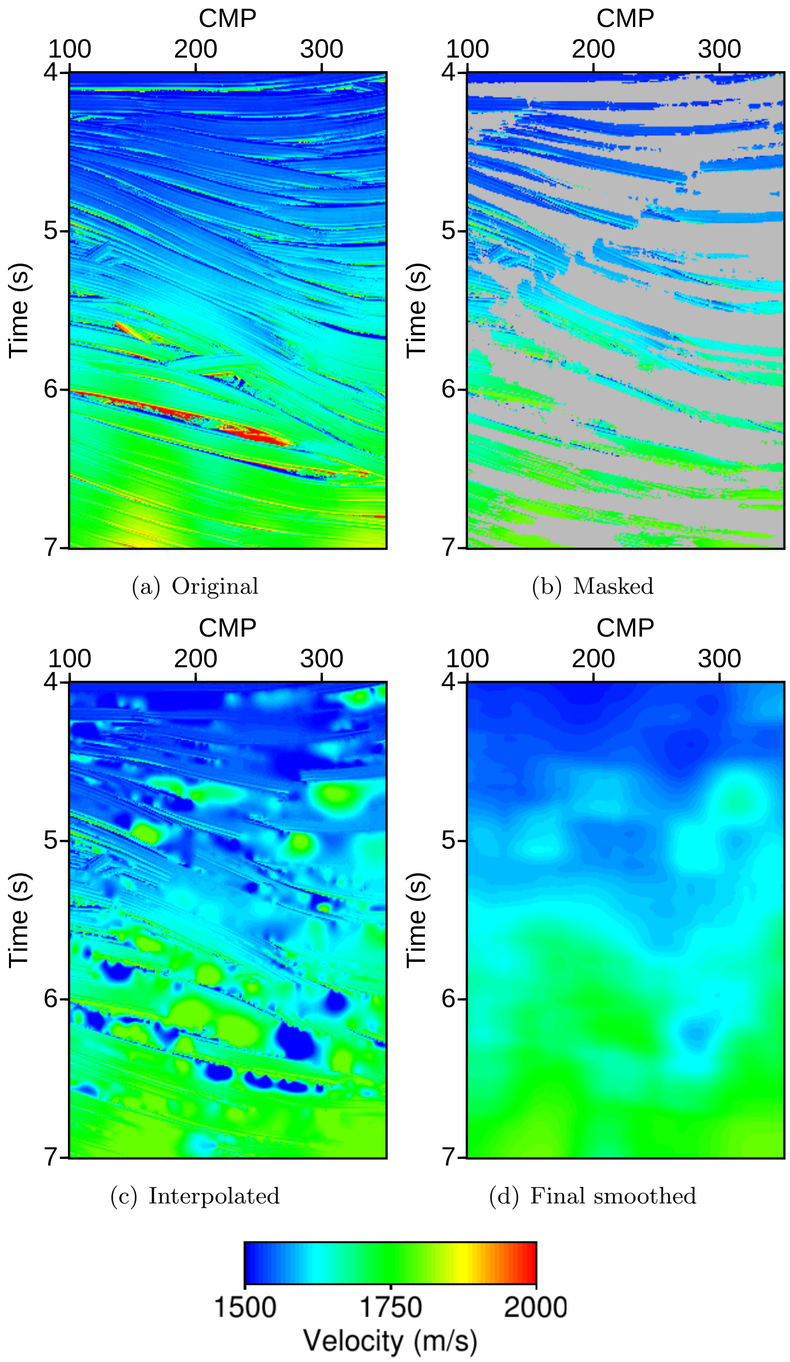

Figure 2.2: Synthetic data. Different steps of velocity refinement, where the colorbar applies to all images. Starting with the original velocity model (a), we masked the section with the weighted coherence (b). Afterwards, interpolation of gaps (c) and smoothing (d) is applied to obtain the refined model.

For a further comparison of the results for the velocity refinement, Figure 2.3 shows common-image gathers (CIG) for CMP 210. The CIG is almost flat for the original velocity model (see Figure 3(a)). Improvements with the refinement Figure 3(b) lead to a reduction of noise at larger offsets, and a more continuous gather. The noise content for larger offsets in Figure 3(a) is due to the calculation of the original velocity model (see equation 2.2), which calculates the velocity for ZO with t_0 and is therefore biased for larger offsets.

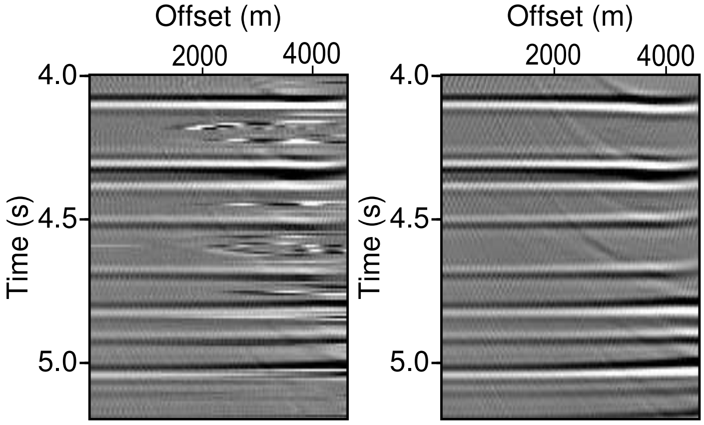

(a) Original (b) Refined

Figure 2.3: Synthetic data. Close-up of CIG for CMP 210. Image (a) shows the CIG with the original used velocity model. After velocity refinement is applied (b) the CIG is cleaner and more homogeneous.

In Figure 2.4 the migration results for the original migrated image (a), the one obtained with the refined velocity model (b), and with the migration deconvolution (c) are shown. Improvements are in particular visible in the fault area. Generally, it can be observed that our suggested strategy for time-migration velocity model building and migration deconvolution results in an improved localization and imaging of faults and a more continuous appearance of reflecting structures. Furthermore, the images of two diffractors are now better focused and clearly recognizable against the image background. For this synthetic data set the advantage of the migration deconvolution is minor, e.g., improved diffraction focusing. Here, we are pushing the limits of time-migration resolution, which is not the case for the field data application. Finally, note that the improved velocity model building and the migration deconvolution were performed in a fully automated fashion.

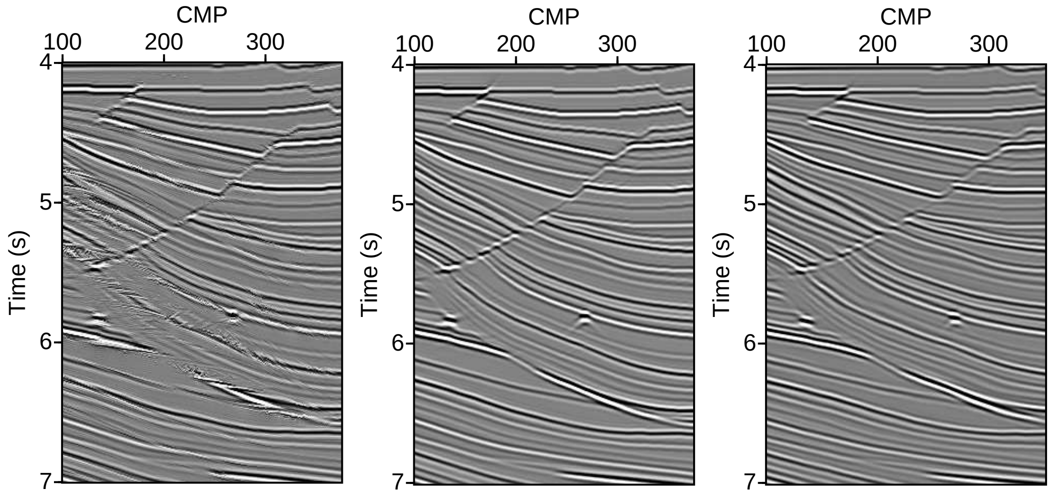

(a) $m_{original}$ (b) m_1 (c) $\hat{m}$

Figure 2.4: Synthetic data. Different migrated sections. The first image (a) shows the migration result with the original used velocity model. Velocity refinement (b) and migration deconvolution (c) improve the image quality.

2.5 Field data examples

We applied the proposed velocity enhancement and migration/demigration loop to a marine and a land data example. The first data set was acquired by TGS in the Levantine basin in the eastern Mediterranean Sea. The Levantine Basin shows a complex seismic stratigraphy of the basinal succession. The deformation patterns of the intraevaporitic sequences include folds and thrust faulting, which provides evidence for extensive salt tectonics and shortening during the depositional phase. Previous works have shown that postdepositional gravity gliding caused salt rollers in the extensional marginal domain, as well as compressional folds, and faults within the Levantine Basin (Netzeband et al., 2006). A subset of the data consisting of around 2000 common midpoint (CMP) gathers with a total line length of approximately 25 km, a shot/receiver spacing of 25 m, a CMP spacing of 12.5 m, and maximum offsets of 7325 m was chosen. The maximum CMP fold corresponds to about 120 traces. The record length was 8 s with a 2-ms sample rate.

Figure 2.5 shows the different steps of the velocity refinement for a subset of the data. Figure 2.5 (a) shows the original velocity distribution calculated from the CRS wavefront attributes. The sedimentary layering is visible, and interrupted by the first ocean-bottom multiple. The image in Figure 2.5 (b) shows the velocity model after application of the coherence filter with a threshold of 0.005. Here, gray corresponds to values below the threshold. In the following step, the interpolation is executed and the result is shown in Figure 2.5 (c). Perturbations caused by the interpolation are less in comparison with the synthetic data due to the more homogeneous distribution of events after filtering. A final smoothing (Figure 2.5 (d)) of the interpolated velocities has to be carried out to perform time migration.

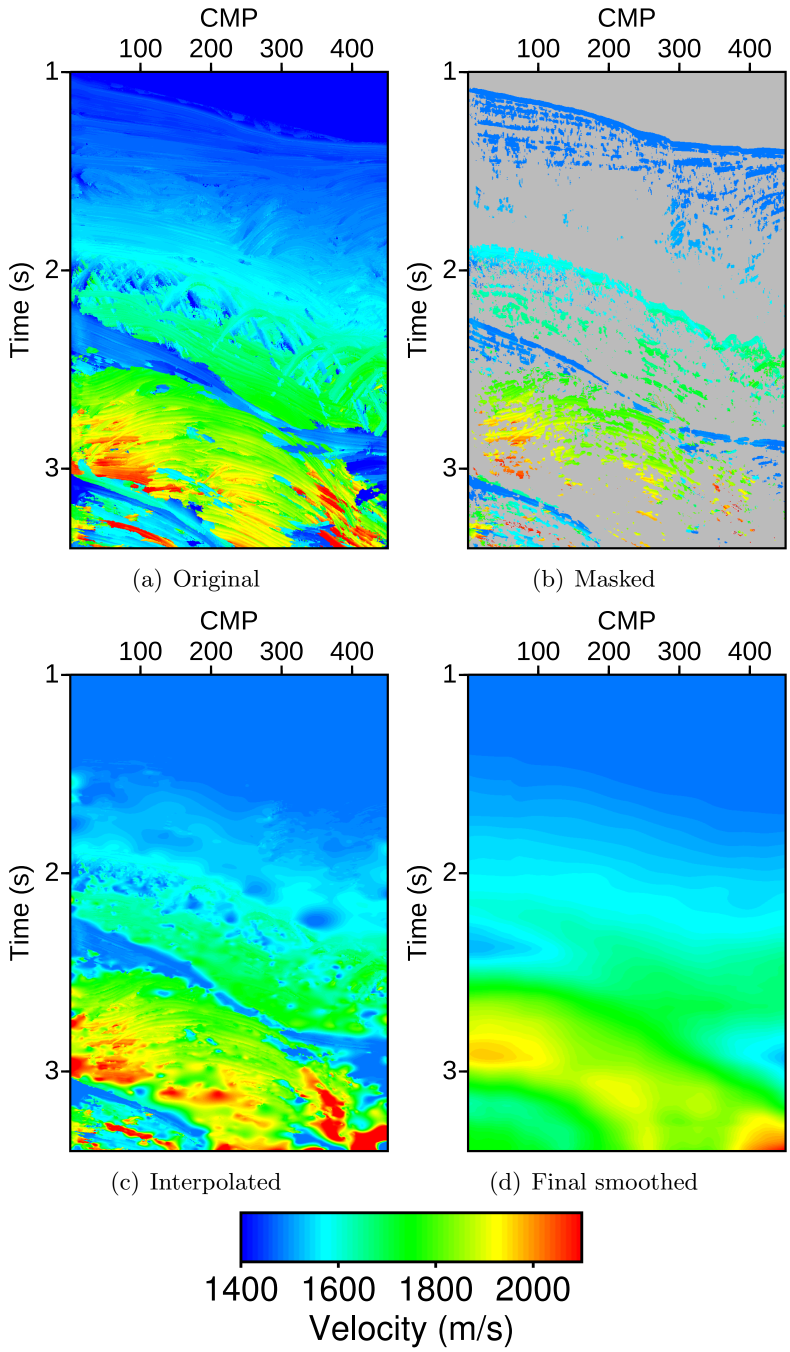

Figure 2.5: Marine data. Different steps of velocity refinement, where the colorbar applies to all images. Starting with the original velocity model (a), we masked the section with the weighted coherence (b). Afterwards, interpolation of gaps (c) and smoothing (d) is applied to obtain the refined model.

Figure 2.6 shows an overlay plot of the automatically generated velocity model and the prestack time-migrated image. The velocity model obtained by coherence filtering and interpolation is smooth and the velocities increase with time except for the first ocean-bottom multiple, which produces lower velocities at larger times, between 2 and 3 s in the lower left corner. The white and red colors indicate higher salt velocities for the triangular structures. There is noticeable consistency of the velocity model with the migrated section not only for the sedimentary layering but also for faults, which start from the triangular structures and continue to the sea floor. The sedimentary layering is horizontally ruptured by a chaotic pattern, which coincides with a slid slump complex (Hübscher and Netzeband, 2007). We also observe low velocities on the bottom of the model. These are likely caused by ocean-bottom multiples which were picked by our unconstrained automatic velocity update.

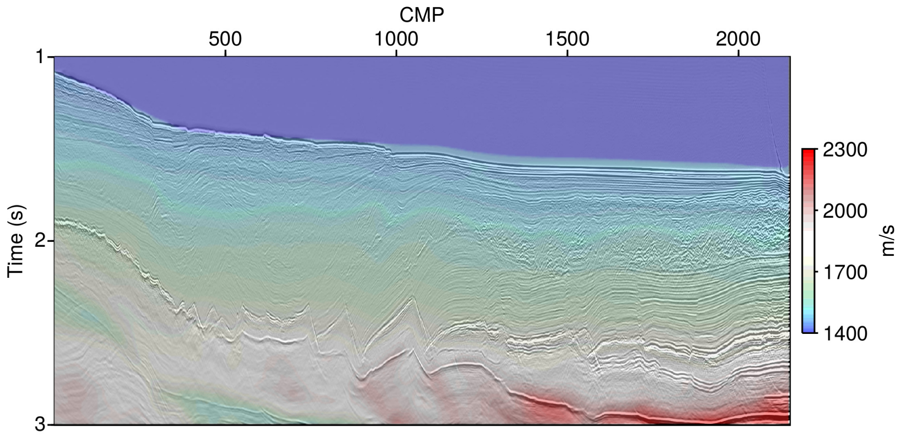

Figure 2.6: Marine data. An overlay plot of the refined velocity model and the corresponding prestack time-migrated section.

To evaluate the results of the demigration, we compare common-offset sections of the original and the demigrated data. Following Hubral et al. (1996), we choose the same apertures and velocity models for forward and backward transformation. The midpoint aperture ranges from 1500 m to 2500 m and the offset aperture from 1000 m to 7000 m. Figure 2.7 shows common-offset sections for $h = 1000$ m, where the original data is presented on the left and the demigrated data on the right. The demigration enhances the data quality and the events are imaged with improved continuity. The second dipping reflection, starting at 1.8 s and the connected diffraction events are both enhanced. Furthermore, structures below this reflection are more visible in the demigrated section. The first ocean-bottom multiple (approximately 2.2 s at CMP 90) is more pronounced too, but reflections below, which are masked in the original data section, become clearly visible in the demigrated section. The automated scheme was able to reconstruct the original data, and improved the resolution of deeper events.

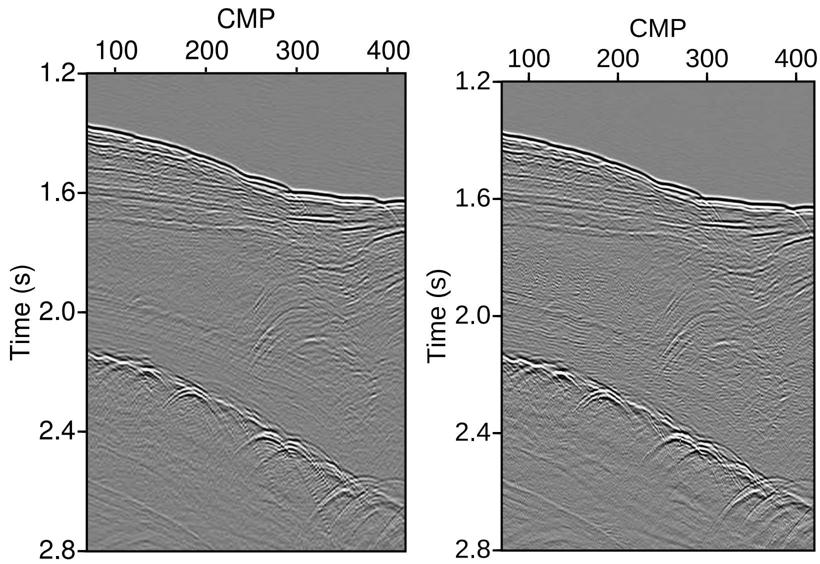

(a) Original (b) Demigrated

Figure 2.7: Marine data. Close-up of common-offset sections: original data (a) and demigrated data (b). Main events are recovered in demigrated image (b).

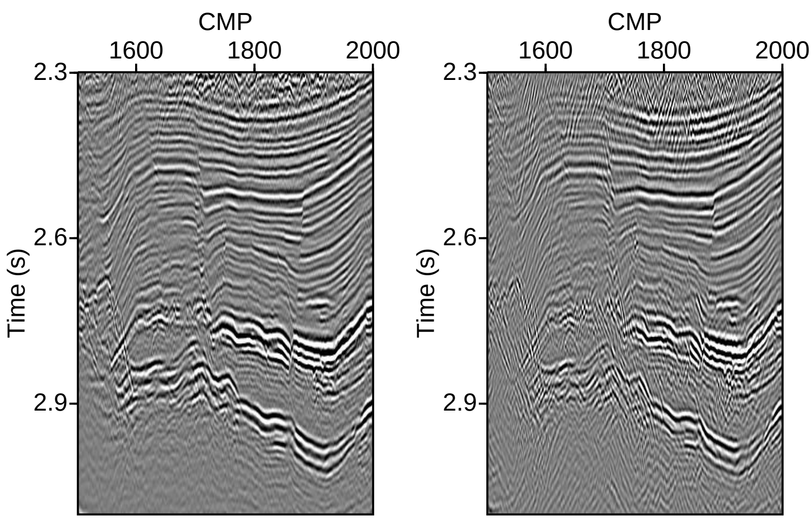

(a) m_1 (b) $\hat{m}$

Figure 2.8: Marine data. Close-up of the migrated sections. Migrated image is shown in (a). The image in (b) calculated with migration deconvolution shows an improved resolution for the middle part.

As the demigration results appear to be reasonable, we can apply the described migration deconvolution. Figure 2.8 shows a close up of two migrated sections. The conventional migration result m_1, i.e., the first image in our deconvolution workflow and the updated migration result $\hat{m}$, i.e., the first image convolved with the inverse of the Hessian, are shown on the left and right, respectively. Note a clearly observable wavelet shortening, i.e., deconvolution, in the updated migration result. We also see an improvement in focusing of diffractions and a better unfolding of bow-ties.

Figure 2.9 displays the remigrated image m_2, i.e., the second image in the deconvolution workflow (a) and the estimated nonstationary matching filters (b). The filter seems to follow the structure – an observation that was also made by Guitton (2004) for the depth case. In time migration, however, a heavily smoothed velocity model is used. Therefore, this is an unexpected feature and confirms an appropriate velocity model.

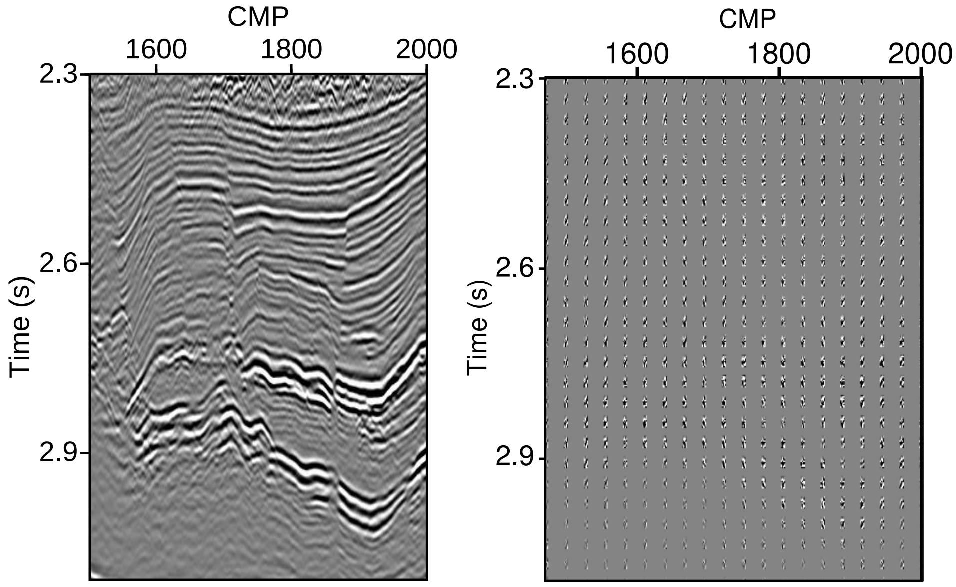

(a) Remigrated (b) Filter

Figure 2.9: Marine data. Close-up of the remigrated section (a) and the estimated filters (b), where the filter follow the structures.

Figure 2.10 displays frequency spectra for the migrated (blue) and the updated (red) image. We observe an expected slight broadening of the spectrum. We also see an unexpected spectrum behavior in the updated image, namely that frequencies higher than 90 Hz, which were artificially boosted by the application of a deconvolution during the processing, became noticeable weaker.

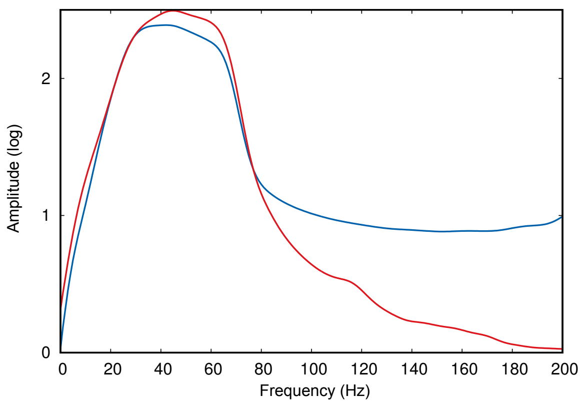

Figure 2.10: Marine data. Frequency spectrum corresponding to the migrated (blue) and the updated (red) image. We observe an expected slight broadening of the spectrum. We also see an unexpected spectrum behavior in the updated image, namely frequencies higher than 90 Hz, which were artificially boosted by the application of a deconvolution during processing, are weakened.

Our second data example is a land data example acquired north of the river Elbe in Northern Germany. It almost coincides with the so called Elbe-Line, and crosses the Central Triassic Graben and its deepest part, i.e., the Glückstadt Graben, perpendicular to the graben axis. Salt structures and complex fault systems characterize the region. The sedimentation process started in the Upper Rotliegend and continued to the evaporites of the Zechstein Group, which reached up to 800 m in thickness. Different phases of salt movements that started in Triassic time formed the salt structures of the region. Each phase is characterized by changing tectonic regimes and different kinds of salt diapirism (Baykulov et al., 2009). The dataset consists of 771 shot gathers with a recording length of 13 s and a sample interval of 2 ms. Explosive sources were used with an average shot spacing of 120 m. For every shot gather, 120 channels with a receiver group spacing of 40 m were deployed. Irregular shooting geometry led to a varying CMP fold, with an average value of 20. A CRS-based data enhancement was applied to the CMP data during the reprocessing in 2007. The CRS-conditioned gathers were used as migration input. In our tests we focused on sedimentary structures and salt plugs, i.e., we mainly considered the time interval from 0 to 6 s two-way traveltime (TWT). We note that the chosen part of the data includes a very complex near-surface region, i.e., in addition to the salt structures, the suggested scheme is confronted with severe weathering effects.

As before, the different steps of the velocity refinement are shown in Figure 2.11. We display the shallow part of the flank of a salt diapir. Figure 2.11 (a) shows the calculated velocities determined by wavefront attributes. Higher velocities are present in the salt diapir, whereas lower velocities are visible at the flanks. The threshold value for the coherence filtering is 0.01 for this data set shown in Figure 2.11 (b). We fixed the near-surface velocity, which was estimated by the processing company, to obtain information for the upper part as well. Small perturbations caused by the interpolation are visible in Figure 2.11 (c). The continuation of layers towards the diapir is still visible. The refined velocity model after a final smoothing is shown in Figure 2.11 (d).

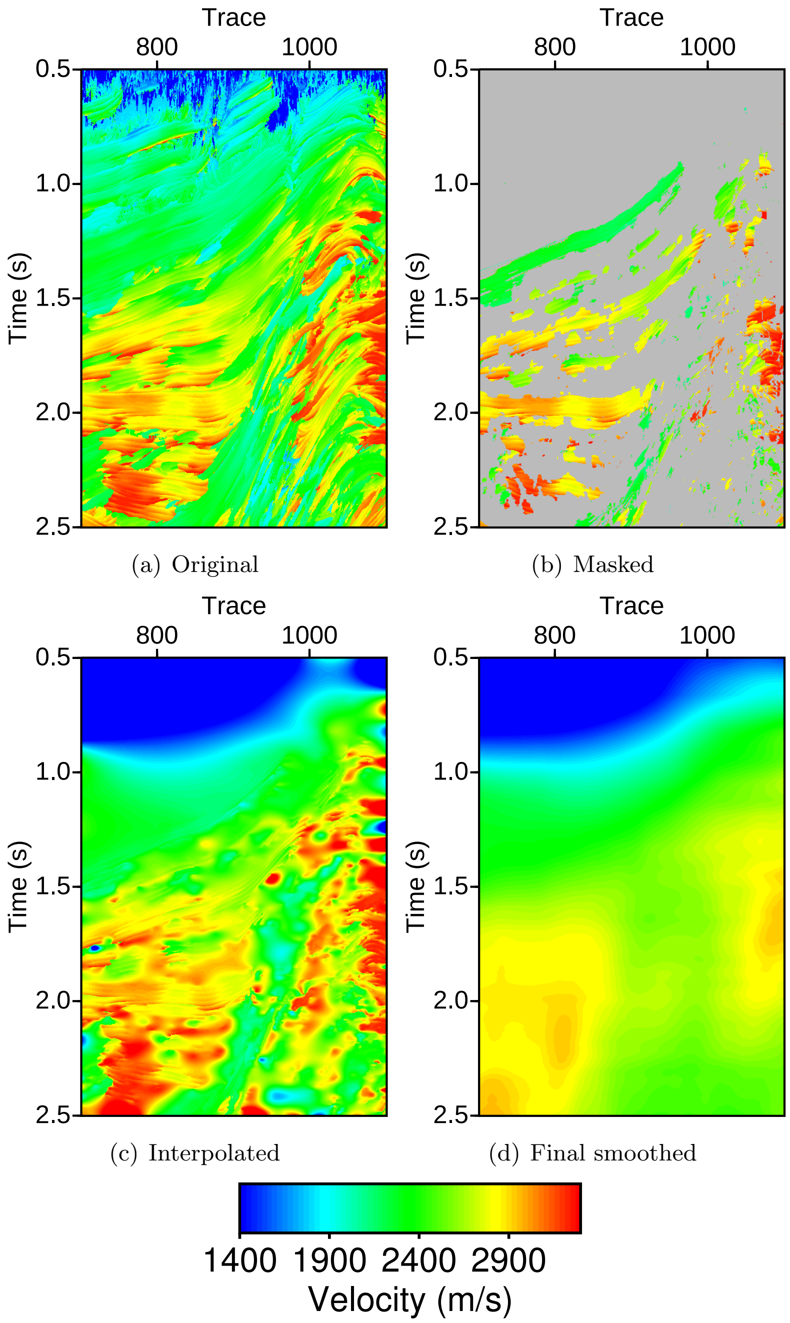

Figure 2.11: Land data. Different steps of velocity refinement, where the colorbar applies to all images. Starting with the original velocity model (a), we masked the section with the weighted coherence (b). Afterwards, interpolation of gaps (c) and smoothing (d) is applied to obtain the refined model.

Figure 2.12 shows the first migrated image m_1 (a) and the second image m_2 (b). It displays a close-up including a complex salt intrusion which almost reaches the acquisition surface, thereby causing complex fault structures in the shallow part of the sections.

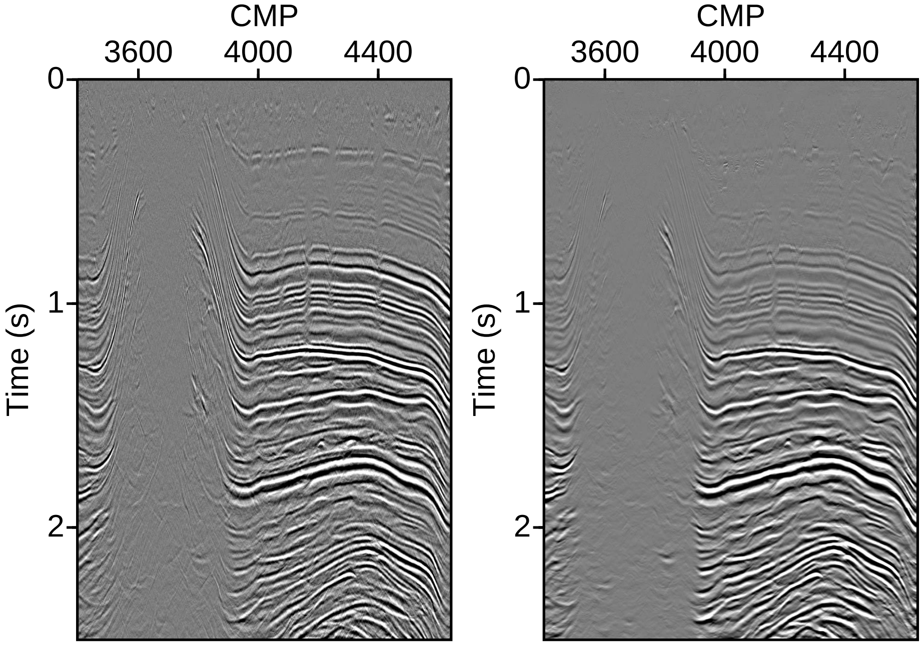

(a) Migrated image m_1 (b) Remigrated image m_2

Figure 2.12: Land data. Close-up of the migrated image m_1 (a) and the second (remigrated) image m_2 (b) including the salt diapir.

In Figure 2.13 the results of migration m_1 (a) and migration deconvolution $\hat{m}$ (b), respectively, are displayed. We notice an increase in resolution. In the near-surface area, we also observe recovery of the weathered layers after migration deconvolution. On the contrary, and as expected, the near-surface reflections after migration are widely destroyed. Somewhat unexpectedly, we observe a recovery of events in the salt region.

Figure 2.14 shows frequency spectra corresponding to the migrated (blue) and the updated (red) image. We observe that the frequency content remains almost the same, with a slight boost of high frequencies between 60 and 120 Hz on the updated image $\hat{m}$. This is an expected behavior due to migration deconvolution.

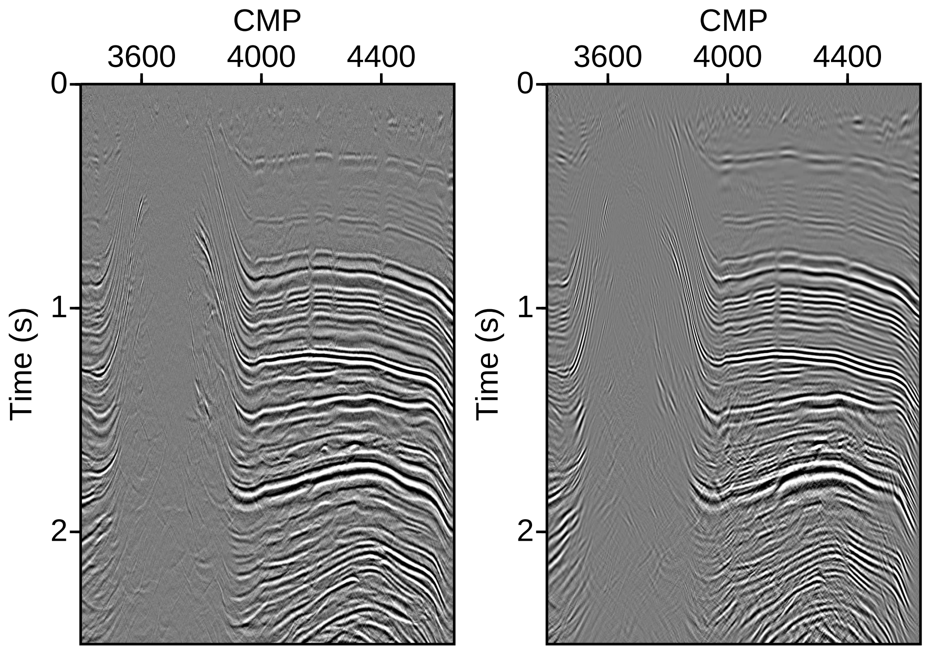

(a) m_1 (b) $\hat{m}$

Figure 2.13: Land data. Result of migration (a) and migration deconvolution (b). We clearly observed an improvement in the event continuity, particularly for near-surface region and somewhat unexpected diapir region. We also recognize a noticeable deconvolution of migrated reflections.

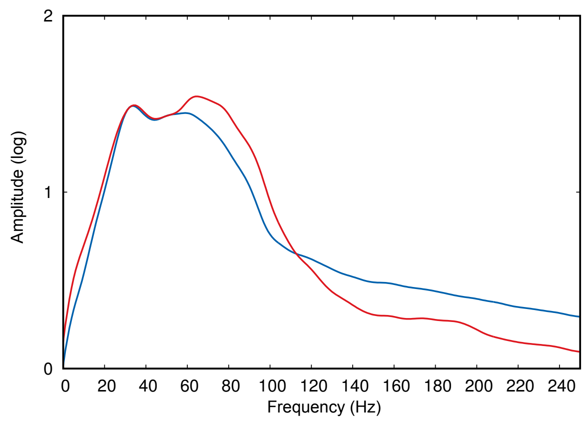

Figure 2.14: Land data. Frequency spectrum corresponding to the migrated image (blue) and the updated image (red). We observe a slight boost of low and high, between 80 and 120 Hz, frequencies due to migration deconvolution.

2.6 Discussion

In this section, we broadly discuss the advantages of the presented time-imaging sequence and address some issues we faced in the process. We recognize that the presented workflow belongs to the family of time-imaging methods, which may reduce its applicability to complex geological systems. However, time imaging is still present in the industry and several attempts have been made to improve it, e.g., by incorporating ray-tracing, extending Kirchhoff migration to higher (up to sixth-order) terms to better account for complex ray paths caused by heterogeneity or anisotropy, application of depth-to-time conversion where depth migration with a well-defined model is performed first and depth images are subsequently converted back to time. In this paper, we firstly addressed the model building of time-migration velocities. The conventional model-building workflow still utilizes seismic reflections only, as time migrations are usually obtained from already existing NMO velocities or through conversion from depth models. Neither of the conventional methods considers diffractions in the modeling, whereas we naturally acknowledge them in this work by utilizing kinematic wavefield attributes extracted for both reflected and diffracted events. We extract the attributes by means of a high-resolution multidimensional, multiparameter data analysis, i.e., we estimate attributes for every data point. A challenge is to determine an appropriate attribute 'de-noising' which is required to obtain smooth velocity models. The use of the coherence filter suggested in this paper may lead to an undesired neglect of weak diffracted contributions in the velocity model building process. Therefore, a careful choice of filter set-ups is required.

One of the drawbacks of time imaging is a transmission imprint on the recorded amplitudes due to the complex wave propagation through the overburden. It can be argued that seismic images (whether in depth or time) are usually not properly recovered by ray-based migration techniques. Only a full-wave migration based on at least a visco-acoustic engine will be capable of performing frequency-dependent phase and amplitude correction of the deteriorated seismic data. Moreover, because of imperfect acquisition, i.e., irregular acquisition sampling, finite recording apertures, and aliased seismic data, a least-squares migration is needed to achieve a better matching of amplitudes in the images. Visco-acoustic least-squares RTM, however, is still not a standard migration algorithm in the industry. The applied migration-deconvolution strategy will certainly not remove all undesired effects of wave propagation. However, we argue that it can help mitigate those effects which are related to imperfect acquisition and incorrect velocity models.

Furthermore, we apply LSM techniques and improve the resolution of the images obtained using the approach described above. Least-squares migration involves a linear modeling/demigration operator L and its conjugate transpose migration operator L'; L operates on model m and L' operates on data d (Nemeth et al., 1999). If L is considered to be Born modeling, L is a volume integral: each contribution to the integral expresses propagation delay from a source to a scatterer (velocity perturbation) to a receiver, followed by bandpass and derivative filtering (e.g., equation 3.2.12 of Bleistein et al. (2001), specialized to zero offset). If L is Kirchhoff modeling, L is a sum of integrals over reflecting surfaces; each contribution expresses propagation delay from a source to a reflecting surface to a receiver, also followed by bandpass and derivative filtering (e.g., equation 5.1.50 of Bleistein et al., 2001).

For both Born and Kirchhoff modeling, L and L' can be discretized as matrices. The cascade of summation and filtering means that (demigration) L is the product of matrices: $Lm = L_1 L_2 m$, where L_1 denotes filtering and L_2 denotes summation of the scattering contributions. For migration, conjugate transposition requires that $L'd = L_2' L_1' d$. That is, bandpass and derivative filtering are applied last in modeling and first in migration. This is important for least-squares time migration.

2.7 Conclusions

We presented a time-imaging method based on a migration/demigration loop. The method comprises an automatic model building (time-migration velocities) and an update of the migrated image (reflectivity). The basis for the forward (modeling) and backward (migration) transformation between different domains is a re-parametrized implicit common-reflection-surface (CRS) approach, which we rewrite in apex coordinates. Exploiting the implicit CRS also allows us to use kinematic wavefield attributes extracted during the high-resolution CRS-parameter analysis.

The benefits of the migration/demigration loop are that seismic data become regularized and enhanced. Moreover, conflicting event dips arising from wavefield interference are naturally handled correctly as migration repositions/removes the dips and the subsequently applied demigration restores them. To further improve the velocity model, we propose to incorporate the coherence section provided by the migration into the model-building process. A coherence threshold is selected and serves as a mask to filter the velocity model which is subsequently interpolated and smoothed. The presented method enhances the velocity models not only in areas assigned to the prominent reflections but also in the vicinity of weaker diffractions.

The duality of migration/demigration operators allows to the formulate time-migration as a least-squares problem. We directly approximate the inverse of the Hessian by nonstationary matching filters. The inverse of the Hessian is then convolved with the migrated image which yields a deconvolved migrated image, i.e., the desired least-squares estimate of the reflectivity model. We do not make any major model assumptions and perform velocity model building and the migrated-image update in a data-driven fashion. Therefore, minimal user interaction is required to carry out both the model and image update. Applications to complex synthetic and field data, acquired off-shore and on land, suggest that the proposed method is capable of noticeably reducing migration swings and recovering amplitudes, thereby leading to improved subsurface imaging in time.

2.8 Appendix: implicit CRS

Vanelle et al. (2010) introduced the implicit common-reflection surface (CRS) stacking approach. The approach is model-based and assumes a circle in the subsurface on which the reflection point $(R \sin\theta, H - R\cos\theta)$ is determined (see Figure 2.15).The traveltime is the sum of t_s, from the source to the reflection point, and t_g, from the reflection point to

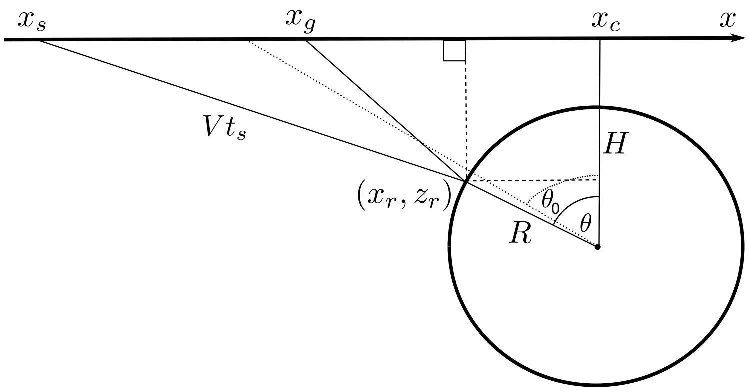

Figure 2.15: Implicit CRS geometry (Schwarz et al., 2014) in source-receiver coordinates. The reflection point is (x_r, z_r). The circle is described by its center point (x_c,H) and the radius R. The dotted lines inidicate the ZO case and denote the starting value θ_0 for the iterative search of the angle θ.

the receiver, respectively:

$$t = t_s + t_g, \quad where \tag{2.9}$$

$$t_s = \frac{1}{V}\sqrt{(x_s - x_r)^2 + z_r^2}, \tag{2.10}$$

$$t_g = \frac{1}{V}\sqrt{(x_g - x_r)^2 + z_r^2}. \tag{2.11}$$

We can solve these equations with the circle equation $(x_r - x_c)^2 + (H - z_r)^2 = R^2$, for a fix middle point x_c, H, where H is the depth of the middle point of the circle, and a constant radius R, so that:

$$x_r = x_c + R\sin\theta \quad and \quad z_r = H - R\cos\theta. \tag{2.12}$$

Now equation 2.9 reads:

$$t = t_s + t_g, \quad where \tag{2.13}$$

$$t_s = \frac{1}{V}\sqrt{(x_s - x_c - R\sin\theta)^2 + (H - R\cos\theta)^2}, \tag{2.14}$$

$$t_g = \frac{1}{V}\sqrt{(x_g - x_c - R\sin\theta)^2 + (H - R\cos\theta)^2}, \tag{2.15}$$

The velocity V is constant. The reflector radius of curvature is R, H denotes the depth to the centre of the circle, and x_c describes the horizontal coordinate of the centre of the circle. It is convenient to change coordinates from source-receiver to midpoint and half-offset with $x_m = \frac{x_g+x_s}{2}$ and $h = \frac{x_g-x_s}{2}$. The reflection traveltime in common midpoint and half-offset coordinates is:

$$t = t_s + t_g, \quad where \tag{2.16}$$

$$t_s = \frac{1}{V}\sqrt{(x_m - h - x_c - R\sin\theta)^2 + (H - R\cos\theta)^2}, \tag{2.17}$$

$$t_g = \frac{1}{V}\sqrt{(x_m + h - x_c - R\sin\theta)^2 + (H - R\cos\theta)^2}. \tag{2.18}$$

The angle θ is determined by an iterative solution scheme. Therefore, we have to set $\frac{\partial t}{\partial \theta} \stackrel{!}{=} 0$ with the solution:

$$\tan\theta = \frac{x_m - x_c}{H} + \frac{h}{H}\frac{t_s - t_g}{t_s + t_g}. \tag{2.19}$$

We start with the angle for the zero-offset (ZO) case $\tan\theta_0 = \frac{x_m - x_c}{H}$ as first guess for the recursive application and are able to solve equation 2.16.
In order to derive a summation time-migration operator, we consider diffractions, where the implicit CRS parameter R vanishes. Accordingly, the diffraction traveltime reads as follows,

$$t_D = \frac{1}{V}\sqrt{(x_m - h - x_c)^2 + H^2} + \frac{1}{V}\sqrt{(x_m + h - x_c)^2 + H^2}. \tag{2.20}$$

We now parametrize equation 2.20 in apex coordinates. This can be achieved by minimizing the diffraction traveltime

$$\frac{\partial t_D}{\partial x_m} = 0, \tag{2.21}$$

with the condition of $h = 0$. The extremum,i.e., the apex is located at $x_m = x_c$ and $t_D = 2H/V$ with the resulting apex coordinates,

$$x_{apex} = x_c, \quad and \quad t_{apex} = \frac{2H}{V}, \tag{2.22}$$

which lead to the time-migration equation in apex coordinates,

$$t = \sqrt{\frac{t_{apex}^2}{4} + \frac{(\Delta x_a - h)^2}{V^2}} + \sqrt{\frac{t_{apex}^2}{4} + \frac{(\Delta x_a + h)^2}{V^2}}, \tag{2.23}$$

where $\Delta x_a = x_m - x_{apex}$ is the midpoint displacement.

3 Denoising migrated data with a deep neuronal network

3.1 Abstract

In recent years, deep learning algorithms have become more and more popular in interpretation of seismic data. In seismic processing however, these algorithms are only starting to be considered. The potential of artificial intelligence and machine learning are currently sparsely used . One important aspect of processing is data denoising. Autoencoder are deep neural networks that inherently denoise and are widely used in many different fields. They aim to find a function that maps data A to data B. We use time-migrated and remigrated images, calculated based on the common-reflection surface (CRS) operator, to train an autoencoder. The remigrated data serves as input (data A) and the migrated data is the target output (data B). The autoencoder contains several layers of convolutional filters and data reductions. The encoder searches for a reduced data representation from the remigrated input image. The decoder uses this representation to reconstruct the migrated output image. The trained network can be used for denoising of migrated images, since unimportant aspects of the data are neglected in the data reduction process. We apply the autoencoder to a land data set from Northern Germany comprising complex salt tectonic. The autoencoder is able to denoise the image and remove imaging artifacts without compromising of seismic events.

3.2 Introduction

Deep learning neural networks (DNN) have become increasingly popular in data analyses over the last years. With the emergence of cheap computational power in the form of GPUs as well as powerful open source libraries, e.g. Tensorflow (Abadi et al., 2016). DNN applications have significantly increased. DNNs are advanced machine learning (ML) algorithms that can be used for a variety of tasks in many kinds of fields, e.g. economy, medicine and geophysics. Traditional machine learning algorithms such as principle component analysis (PCA), support vector machines (SVM) or self organizing maps (SOM) are well established but have limitations. The scientific community is still just exploring the possibilities of artificial intelligence (AI), which machine learning belongs to.

AI can improve and speed up the whole chain of seismic data processing. Especially, interpretational steps use different ML techniques. Wang et al. (2018) give an overview about recent years applications. In data acquisition and processing, the seismic community starts to use different ML techniques as well. The field of processing has a great potential for ML applications and is not yet as good explored as interpretation, e.g., for fracture

characterization or salt body detection (Di et al., 2018; Shi et al., 2018).
There is a large potential to combine ML with processing, e.g., migration. Time migration is a widely used tool for subsurface imaging because of its computational speed, robustness, and decreased sensitivity to velocity errors if compared with depth migration. A focused time migrated image requires appropriate time migration velocities and provides distorted results when the subsurface structure is too complex.

An important aspect of seismic data processing is denoising. This is a well investigated and important issue. Treitel (1974) introduces so-called, complex Wiener filter for seismic data and Canales (1984) expand this concept to the well-known f-x deconvolution. An overview in seismic denoising is given by Yilmaz (2001). More advanced techniques are presented during the last years, e.g., Bonar and Sacchi (2012) adapt non-local means filter for reflection image denoising, Beckouche and Ma (2014) use the dictionary learning method for data denoising. Agostinelli et al. (2013) show an approach for medical image denoising. Medical images are very close to seismic data and a lot of techniques can be adopted from this field for seismic images. Vincent et al. (2010) use an autoencoder for denoising of different data sets, such as, MNIST (hand-written numbers) and natural scene images. They train a deep neuronal network to reconstruct the image and account for noise.

We present a similar approach for migration denoising using a deep convolutional neuronal network organized as a supervised autoencoder. Autoencoder networks encode data into a reduced representation and use this reduced representation for different applications, e.g. reconstruct data or classify data in segmented maps.

Hubral et al. (1996) and Tygel et al. (1996) present an imaging theory based on migration and demigration in depth. Iversen et al. (2012) present a time-based approach. These approaches use the duality of modeling (demigration) and imaging (migration) (Claerbout et al., 1996). On the one hand, time migration sums traces to focus events, unfolds triplications, collapses diffractions, and handles conflicting dips. On the other hand, time demigration performs a semicircle data spreading with superposition to model the seismic data.

We make use of the duality of modeling and imaging to obtain a migrated and remigrated image as input and labels for the deep NN. The network consists of a series of convolutional filters and data reductions (encoder) for data analysis and convolutions and upscaling (decoder) for data reconstruction. The aim of the encoder is to find a representation which describes a remigrated image. The decoder uses the encoded features to reconstruct the original migrated image. The essential aim is to find a function that maps remigrated data to migrated data. The successful application of such a network reduces the noise automatically, due to the autoencoder structure. We train and test the deep NN with complex land data. With the suggested approach, we perform image processing to improve the quality of the migrated image.

3.3 Method

We use remigrated images as input and migrated as target output in an autoencoder to obtain a reconstructed denoised image from the deep NN. Contrary to the denoising done by the remigration, the denoised image of the NN has no operator noise, as no specific

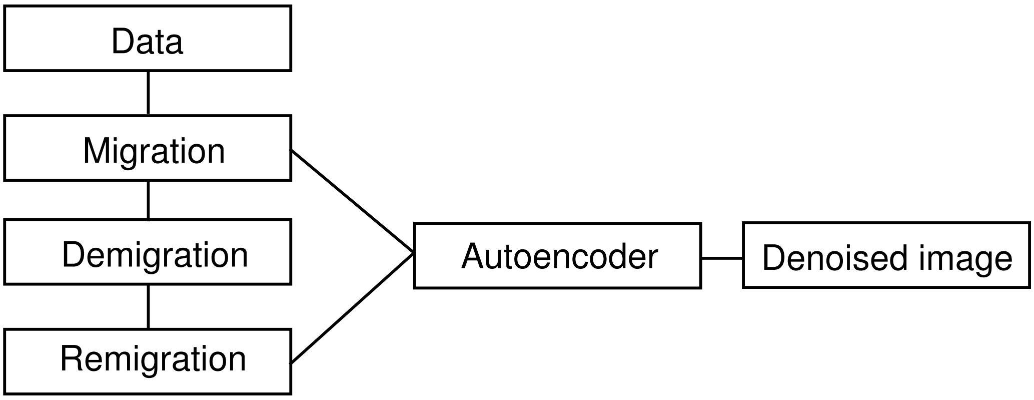

Figure 3.1: Sketch of the proposed method to obtain a denoised image with the use of a deep neuronal network.

operator is involved, among other advantages discussed later. A sketch of the proposed work flow is shown in Figure 3.1. When we write re-/migrated images, we mean migrated offset images, such that, migration is only performed in midpoint direction, comparable with common-image gathers (CIG). The underlying theory for migration/demigration and for the deep NN is explained in the following paragraphs.

3.3.1 Migration and demigration

The proposed method uses migrated images as input for the neuronal network. Migration and demigration build a loop in geophysical modeling (Claerbout et al., 1996). The modeling operator with respect to reflectivity is referred to as demigration and uses linear operators. The inverse is referred to as true-amplitude migration and uses linear operators, too. In this paper, we use implicit the commom-reflection surface (CRS) operator (Schwarz et al., 2014) for both tasks, modeling and inversion. The implicit CRS is a multi-parameter stacking operator controlled by wavefront attributes (Hubral, 1983) and can be formulated for migration. To do this, local apex coordinates are introduced. We use the diffraction variant of the operator for migration in terms of apex coordinates:

$$t = \sqrt{\frac{t_{apex}^2}{4} + \frac{(\Delta x_a - h)^2}{V^2}} + \sqrt{\frac{t_{apex}^2}{4} + \frac{(\Delta x_a + h)^2}{V^2}}, \tag{3.1}$$

where $\Delta x_a = x_m - x_{apex}$ is the midpoint displacement, h is the half-offset, t_{apex} is the apex traveltime, and V is the time-migration velocity. Schwarz et al. (2014) relate the kinematic wavefield attributes (Hubral, 1983) with the time migration velocity:

$$V = \frac{v_{NMO}}{\sqrt{1 + \frac{v_{NMO}^2}{v_0^2}\sin^2\alpha}} \quad \text{with} \quad v_{NMO} = \sqrt{\frac{2v_0 R_{NIP}}{t_{apex}\cos^2\alpha}}. \tag{3.2}$$

The near-surface velocity v_0 is assumed to be known. Furthermore, the are two kinematic wavefield attributes α and R_{NIP} required, which denote the incidence angle of an emerging wave at the surface and the radius of curvature of a hypothetical wavefront starting at normal-incident point (NIP) in the subsurface. The attributes are determined by fitting the implicit CRS operator to the pre-stack data. We observe an automatic dip correction for time-migration velocities by considering the incidence angle in equation 3.2.

Equation 3.1 is a double-square root expression and resembles a conventional Kirchhoff migration traveltime, e.g., (Yilmaz, 2001). To obtain the corresponding modeling operator for demigration, we solve equation 3.1 for t_{apex}:

$$t_{apex} = \sqrt{t^2 - \frac{4(\Delta x_a^2 + h^2)}{V^2} + \frac{16\Delta x_a^2 h^2}{t^2 V^4}}. \tag{3.3}$$

This equation is a single-square root expression. To obtain the remigrated image, we apply migration to the demigrated data. Both expressions, migration and demigration, are also valid for the poststack case, where the half offset h vanishes. In perfect condition migration and demigration are inverse operations. However, velocities are not exact nor do events match the hyperbolic operator.

The migration/demigration loop is executed with the adjoint operators because the real inverse is difficult to calculate. Due to this fact a subsequent remigration of the demigrated pre-stack data leads to small deviations in the image compared to the migrated image. The process of demigration leads to a noise reduction.

3.3.2 Deep convolutional neural network

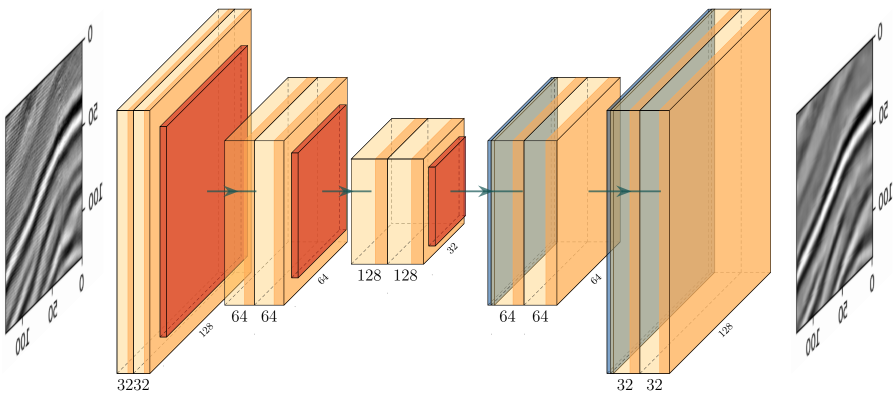

Figure 3.2: Structure of the autoencoder network used in this work.

In our work, we aim to automatically decrease the noise content of a migrated image with the help of a remigrated image. To achieve this goal, we apply a deep supervised neuronal network. From a mathematical point of view, we are considering a regression problem, finding a function to map remigrated data to migrated data. The applied autoencoder has ten convolutional layers, four max-pooling layers, and is a simplified version of the U-net by Ronneberger et al. (2015). The U-net was designed for image segmentation in electron microscope stacks and performs particularly well, when a very limited amount of data is available (Arganda-Carreras et al., 2015). Since seismic data is smooth and images rather simple in structure, complex architectures were not performing better. In fact, they are much harder to train, since more unknowns are involved, which may lead to instabilities. For that reason, complex networks are also more prone to overfitting . The network structure is shown in Figure 3.2.

A convolutional layer contains M different filters of NxN samples, applied to every sample of the input to a layer, e.g. 64 different filters of size 3x3 are convolved with the input of the layer (usually split into so-called batches to fit on GPU memory). The max-pooling reduces the data and keeps only the most significant sample of a small area (in 2D the area has 2x2 samples). Furthermore, batch normalization is applied a) leading to an input which is comparable throughout the whole network, b) allowing higher learning rates, which speeds up the computation, and c) reduces the problem of overfitting. We further account for the overfitting problem by making use of data augmentation to increase the valuable amount of data. In general, overfitting leads to the problem that we cannot use one trained network for a general task (Goodfellow et al., 2016). As loss function we choose the Huber loss (citation needed!), which combines L1 and L2 norms, and is often used for regression tasks with NN.

Each image passes through the whole network for encoding and decoding to ensure that all information is available in the deepest layer of the encoder. In case of successful mappings, the network has learned how to translate an input image to a target output.

3.3.3 Training and data augmentation

The network is designed such, that it takes 2D images (CIG) from the 3D data cube (time, common-midpoint and offset). To reduce the memory required and better randomize patterns seen by the NN, we randomly determine a certain amount of samples from the input data and cut out a defined area around the sample in time and common-midpoint dimension. This results in a few small 2D images used per batch. The autoencoder works with this 2D images of the remigrated data and predicts a small 2D image which is compared to the according migrated data. The misfit is minimized to train the neural network. This procedure is done iteratively until the given number of iterations is reached. In our case we used a total of 2 million iterations with a batch size of 64 samples per iteration. Therefore, the network has seen a total of 128 million samples, while the data consists of 5 million samples. Hence, we used approximately 25 epochs.

The first run uses clean, e.g. no boundary effects, near-offset images to get a first subset of filters. The training on the small excerpt of the original data is used to get reasonable initial filters, that are refined using all available data.

The second run uses these filters for additional training with all offsets including boundary effects, which leads to a higher noise content.

For the third run, we try different data augmentation techniques to increase the amount of valuable data. This feature is important for the case of limited data and can avoid the problem of overfitting. Data augmentation can be roughly divided into two parts: geometrical and optical augmentation. Geometric augmentation covers techniques, such as, scaling, rotation, and flipping. Optical augmentations include , e.g., changes in brightness, contrast, hue, and saturation. Furthermore, different kinds of noise can be used for augmentation. We test four augmentation techniques, namely brightness, contrast, flipping, and rotation, to evaluate the benefit of each one for the NN. The used augmentation techniques are applied separately in a random fashion, e.g., the brightness is randomly changed in a predefined interval. The same applies for a change in contrast. The flipping is performed from left to right or top to bottom and is likewise steered by a random factor. The rotation is performed in steps of 90 degrees. The final amount of rotation is again steered by a random factor.

3.4 Results

We apply our method to a land data set acquired north of the river Elbe in Northern Germany. The line, which is part of the Central Triassic Graben, crosses the Glückstadt Graben perpendicular to the graben axis. Complex salt tectonics, e.g., diapirism, and fault systems characterize the region. The profile consists of 771 shot gathers with a spacing of 120 m. Maximum offsets of 4800 m are provided by 120 channels with a geophone spacing of 40 m. Total recording time is 13 s with a sampling interval of 2 ms. The sedimentary structures and salt features are located in the first 6 s two-way traveltime (TWT). We use CRS-based enhanced and regularized pre-stack data (Baykulov and Gajewski, 2009) due to the small mean fold of 20, and the irregular shot line of the original pre-stack data.

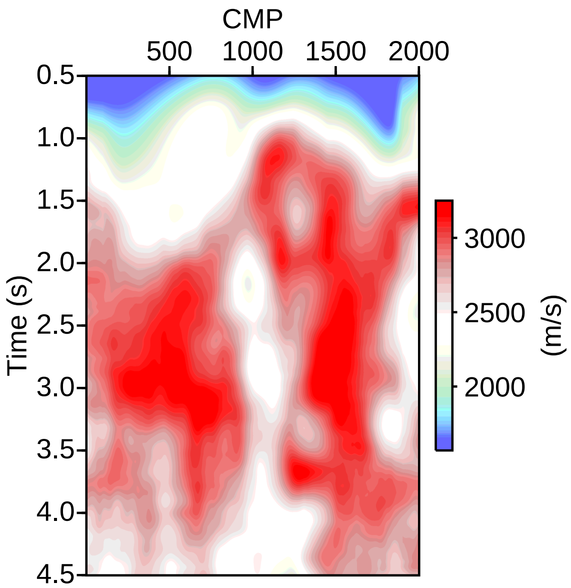

Figure 3.3: Velocity model used for migration.

Wavefront attributes determined from the the data were applied to obtain time migration velocities (see Figure 3.3), where we consider a procedure proposed by Glöckner et al. (2019a). They use the coherence of the migrated image as weight for the velocities. Interpolation of gaps and smoothing are applied to obtain a refined velocity model for time migration. Higher velocities (red) indicate salt diapirs which are typical for this region.

Figure 3.4 shows the CIG for common-midpoint (CMP) 800. The gathers are flat in the middle part of the images, which means that the velocities are consistent with the data.

The remigrated image b) shows less noise in comparison with the migrated image a). The enhanced signal-to-noise ratio results from the migration/demigration loop. CIG for the deeper part of the data are not flat, especially, larger offset gathers are not aligned. A reason for this is, that the velocity model was obtained for zero-offset and applied for the full offset range without adaption.

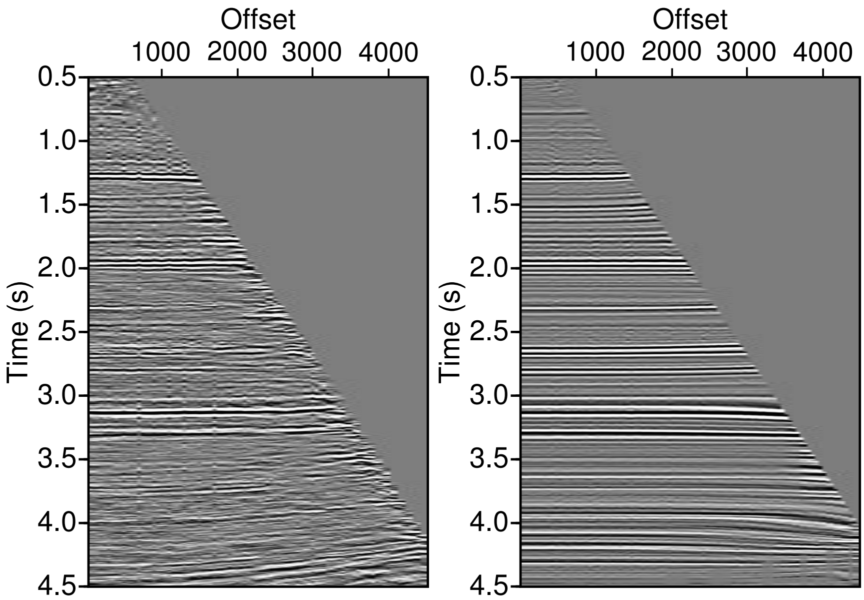

(a) CIG migrated image (b) CIG remigrated image

Figure 3.4: Common-image gather for CMP 800.

Figure 3.5 shows an intermediate step of the training process of the autoencoder. The size of the images is given by an user-defined value, which is 64 samples in our case. In principle, it is possible to use varying image sizes as well. The NN needs to find a method how to reconstruct the migrated image b) from the remigrated input image a). Therefore, different filters are tested to reconstruct images c). We choose an example from iteration 1.95 million in the second run, where the training is nearly completed. The reconstructed image c) is similar with the migrated image b), as requested, and the noise content is reduced in comparison with the migrated b) and remigrated image a).

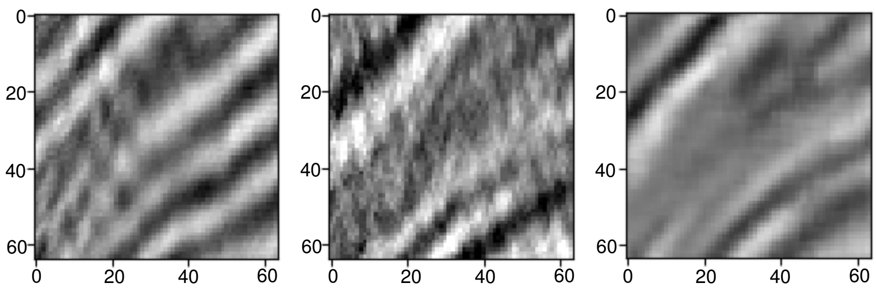

(a) Remigrated image (b) Migrated image (c) Reconstructed image

Figure 3.5: Reconstruction from autoencoder after 1950000 iterations of second epoch.

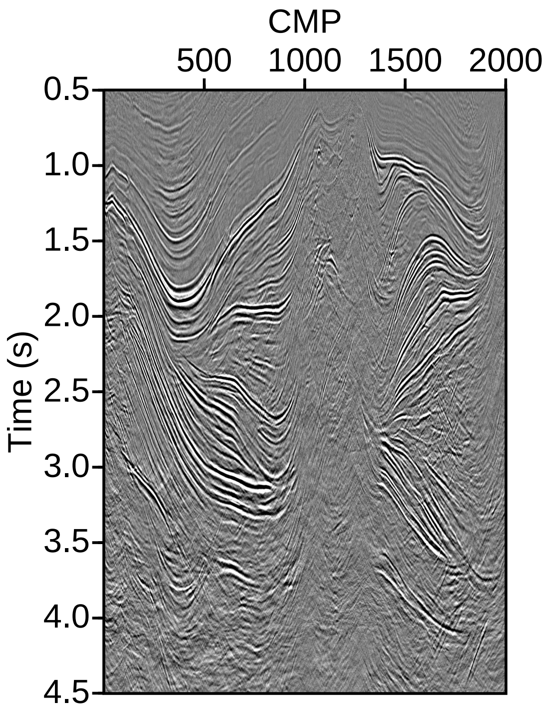

(a) Migrated image

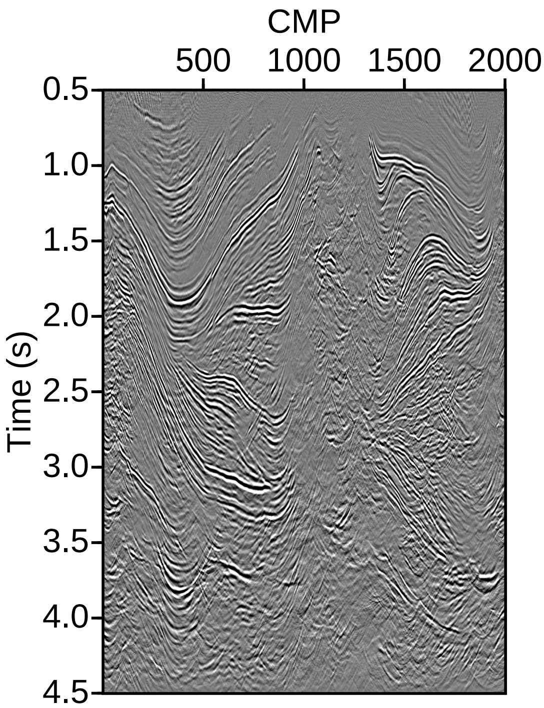

(b) Remigrated image

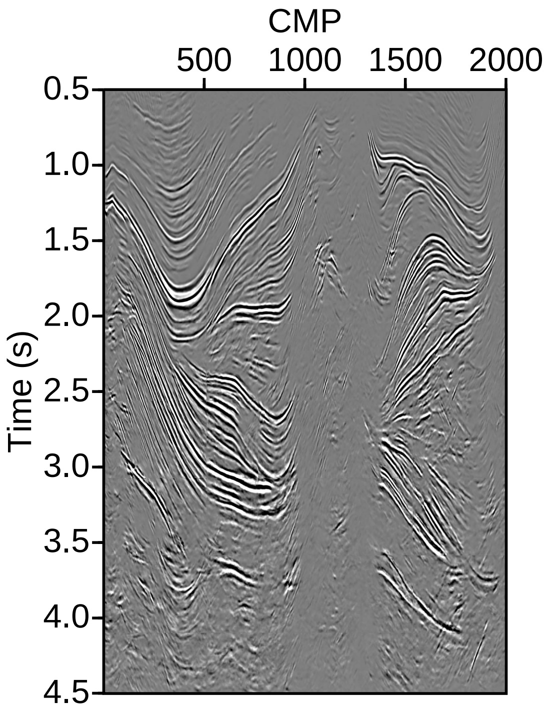

(c) Denoised image

Figure 3.6: Time migration results showing the improvements of autencoder for denoising.

Figure 3.6 shows the different migrated images. The denoised image c) is shown without data augmentation. The block like appearance of the denoised image is a result of the the chosen filter size. The migrated images show a salt diapir between CMP 1000 to 1400 and folded structures between different salt diapirs. The remigrated image b) shows the most features in the salt diapir but the noise content is high, too. The denoised image c) shows a decreased noise content, especially in the upper part and in the salt diapir. Furthermore, the cross-shaped noise, which is introduced by the CRS operator, in the lower part of migrated and remigrated image is reduced. Another interesting observation , e.g., CMP 800 at 2.6 seconds is that the autoencoder suppresses migration smiles.

Figure 3.7 shows a close-up of the right salt flank with different techniques used for data augmentation and no augmentation. Similar to before, the block like appearance of the images is a result of the the chosen filter size. The migrated image a) and denoised image b) with augmentation are shown for comparison. The different tested augmentation techniques show similar results. Small deviations are present in the inner structure of the salt diapir between CMP 1000 to 1300. Further small differences are visible in the lower right part which contains folded sediment layers. The denoising characteristic after augmentation is comparable with the noise content after the second epoch, Figure 3.7 b).

Concerning the augmentation the second close-up (Figure 3.8) shows the left salt flank of the salt diapir with similar results as before. The different augmentation techniques display differences in a very small range. Differences can be found between 2.6 and 2.9 seconds and CMP 700 to 800, where the sedimentary layering is not continuously imaged.

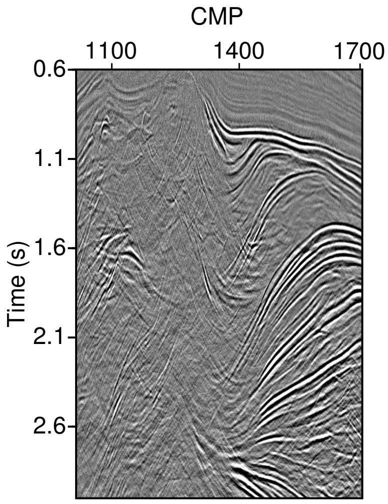

(a) Migration

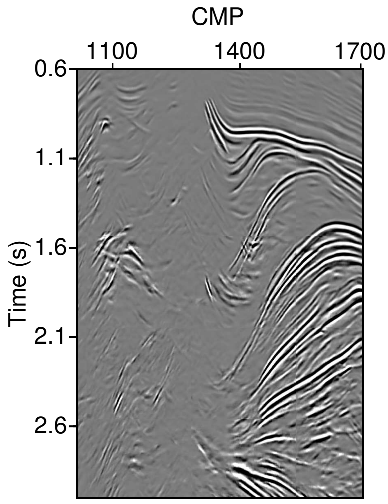

(b) No augmentation

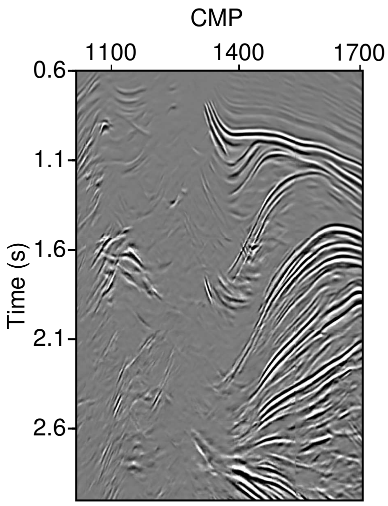

(c) Random brightness

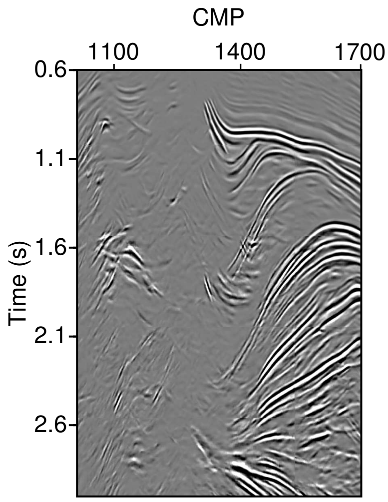

(d) Random contrast

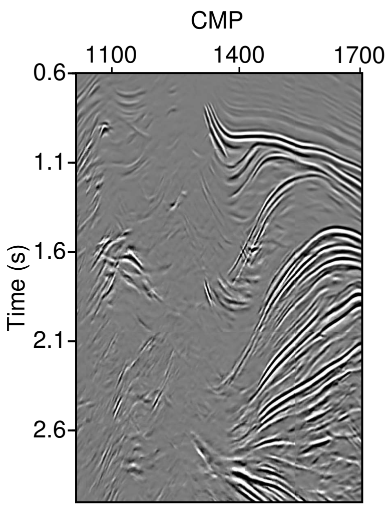

(e) Random flipping

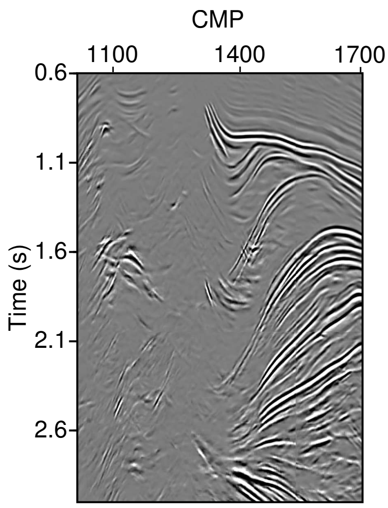

(f) Random rotation

Figure 3.7: First close-up of the right salt flank. Comparison of the different data augmentation techniques.

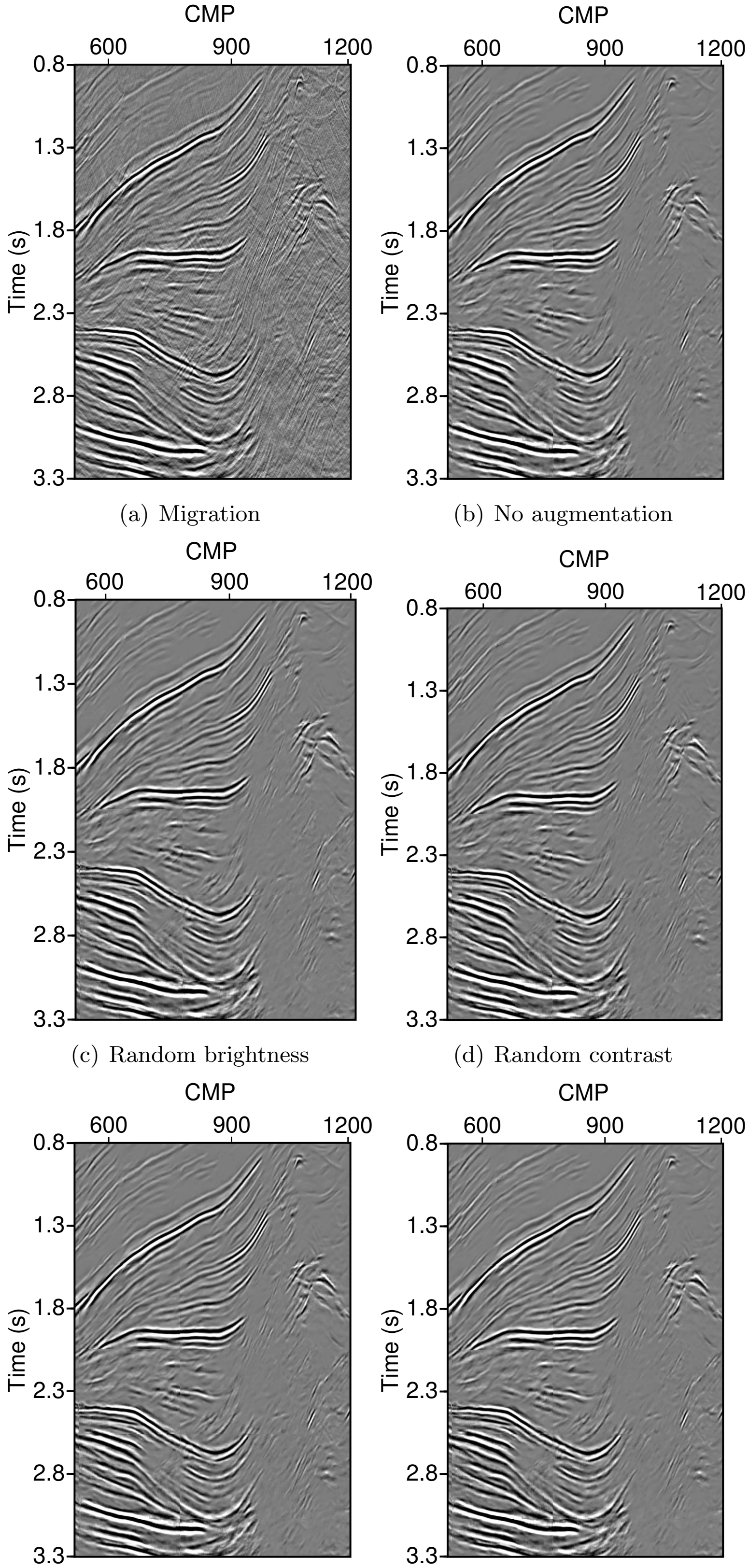

(a) Migration (b) No augmentation

(c) Random brightness (d) Random contrast

(e) Random flipping (f) Random rotation

Figure 3.8: Second close-up of the left salt flank. Comparison of the different data augmentation techniques.

Figure 3.9 shows a close-up of the near-surface layering. This area is affected by weathering effects and it is difficult to determine an appropriate velocity model for migration/remigration. Nevertheless, the autoencoder (denoised image c)) was able to reconstruct layers and decrease the noise content, especially in comparison with the remigrated image b). Structures are better visible in the denoised image c) in comparison with the migrated image a).

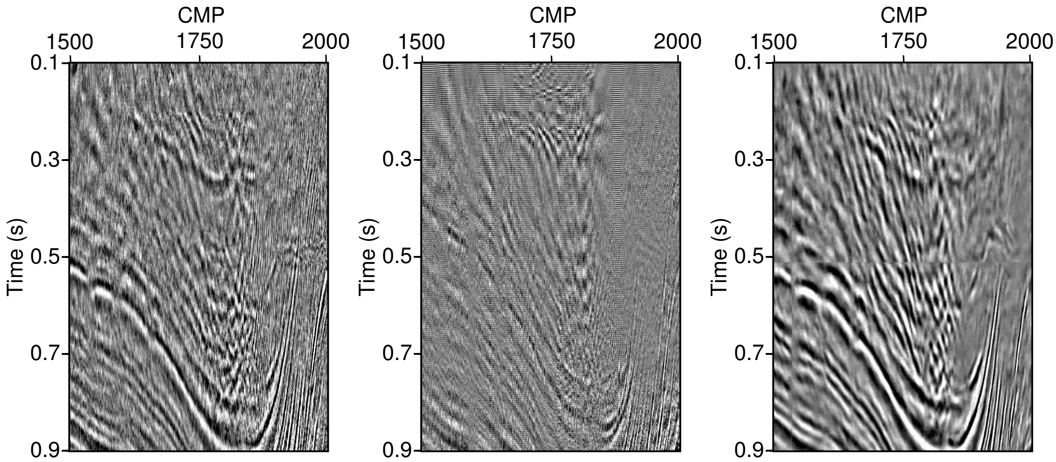

(a) Migration (b) Remigration (c) Denoising

Figure 3.9: Third close-up of near-surface layering, which shows the potential reconstruction of layers with autoencoder for shallow part of the data.

Figure 3.10 shows difference plots of the migrated and denoised image without augmentation for the two close-up areas. We normalized the amplitudes between -1 and 1 for a better comparison because the autoencoder is not designed to reconstruct true amplitudes. However, it is possible to do so when tracking normalization operations, particularly before feeding the data into the network and applying the inverse scaling. The lower part of the left salt flank a) shows the largest deviation in amplitude in the total data set. The major part of the data however, is well reconstructed where most events are well recovered and mostly noise is filtered out because no coherent events are visible in the difference plots.

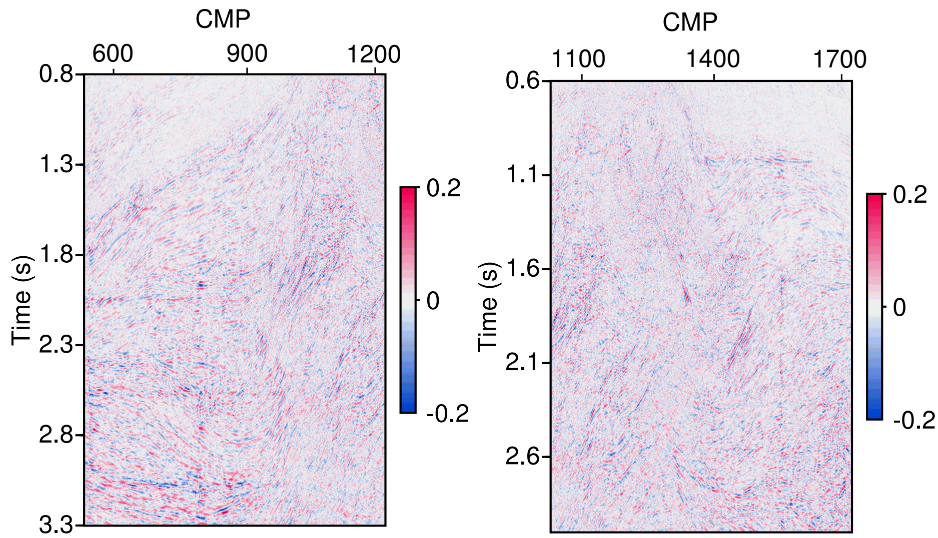

(a) Left salt flank (b) Right salt flank

Figure 3.10: Close-ups of the difference plot between migrated and denoised images with normalized amplitudes.

3.5 Discussion

Autoencoder are widely used for image denoising. Vincent et al. (2010) show different tasks, where autoencoder are used to denoise different kind of images. Here we presented the application to migrated seismic data as a possible tool for denoising.

In this work, we focus on time migration. However, the proposed denoising work flow is applicable to depth migrated images as well since the network just looks at 2D images. Depth migration is more involved because of computational costs and requires a more accurate velocity model in comparison to time migration.

Another aspect covered in this work is data augmentation. Data augmentation is a useful tool to increase the amount of meaningful data if not enough training data are available. It can further decrease the issue of overfitting and helps to generalize the trained NN. For the data used in this work, apparently the amount of valuable data is sufficient because no major visible improvements in denoising are achieved with data augmentation. Based on this observation, we conclude that we designed an appropriate deep NN for the task of denoising. Therefore, we suggest to stop training after the second run and apply the trained deep NN to the total data set. Nevertheless, data augmentation could be an important tool in the case of transfer learning.

To investigate the issue of overfitting, it would be interesting to test the trained deep NN with other data sets with a similar geology. The ideal result would be a comparable noise reduction as observed in the presented work. Nevertheless, the trained NN just learned the special characteristics of the presented data set, like, the salt diapirs and the associated sedimentary layering. The denoising ability for other features in data sets is not yet investigated to determine whether this trained NN can be applied to data from similar geological environment or whether one has to train a new one.

In general NN tasks can be split in two groups, classification and regression. It is easier to estimate the performance of a classification task in comparison with regression, particularly for supervised data. Different tools to define the correct and incorrect percentage of classifications are available, like the F-score (Sorensen, 1948; Dice, 1945) and confusion matrices (Powers, 2011). This is more difficult for regression tasks. The often used decrease of loss function per iteration for the evaluation of performance and convergence is difficult in our case. Figure 3.11 shows the mean-squared error of the loss function for our NN. Due to the large variance within the data, it is not obvious, how many iterations are needed until a sufficient convergence of the loss function is reached and iterations could be stopped. It is possible that a similar result in terms of denoising ability can be achieved with fewer iterations than the here proposed two million iterations. An appropriate criterion has to be found for this issue. So far, we are not aware of an appropriate method to optimize the number of iterations in such cases.

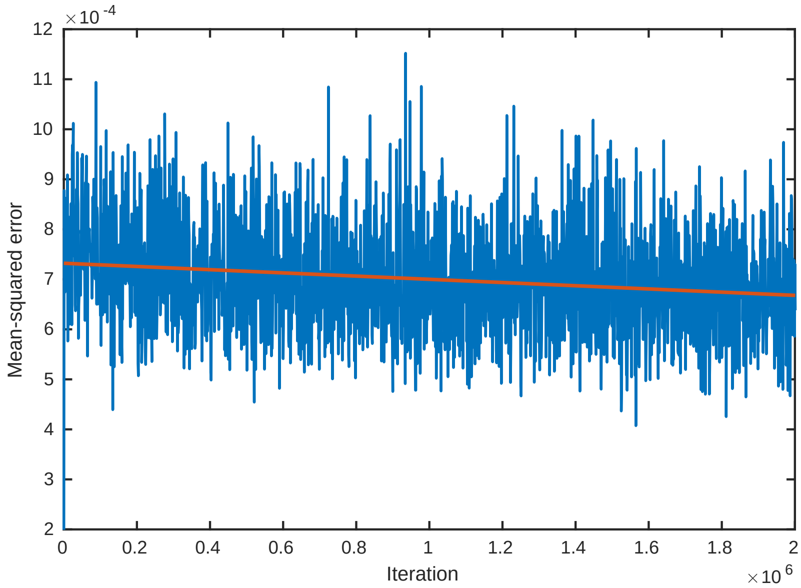

Figure 3.11: Mean-squared error of loss function for second epoch. The error is plotted every thousandth iteration in blue. The red line denotes the regression line.

3.6 Conclusion

We presented a work flow for denoising migrated images, based on a convolutional neural network. The input of the deep neuronal network are time-remigrated images. Our approach is a supervised approach, where migrated images serve as according labels. We calculate these images with the implicit CRS time migration and demigration operator, which is similar to a Kirchhoff migration and demigration. The used a deep neuronal network, an autoencoder, which is designed to reconstruct an image and reduce the noise. Several convolutional and max-pooling layers encode the most important features of the data and reduce the input image in size. The following decoder reconstructs a label, in our case the migrated data, from this reduced features. This procedure implicates an automatic noise reduction due to the structure of autoencoders. We train our deep neuronal network and test different data augmentation techniques, such as, change in brightness and contrast, and different flip options and rotations. We apply the autoencoder to a land data set in Northern Germany with complex salt tectonic features. The denoised image shows a reduced noise content and reconstructs all prominent events. Important noise sources, e.g., operator induced noise, migration smiles, and random noise are suppressed. Additional different data augmentations do not improve the quality of the image or further reduces the noise. Nevertheless, data augmentation is an important tool if not enough valuable input data is available or in the context of overfitting. The problem of overfitting does not seem to be an issue in our study, which means conversely, an appropriate network design.

4 Imaging zero-offset 3D P-cable data with CRS method

4.1 Abstract

Standard seismic acquisition and processing require appropriate source-receiver offsets. P-cable technology represents the opposite, namely, very short source-receiver offsets at the price of increased spatial and lateral resolution with a high-frequency source. To use this advantage, a processing flow excluding offset information is required. This aim can be achieved with a processing tuned to diffractions because point diffractions scatter the same information in offset and midpoint direction. Usually, diffractions are small amplitude events and a careful diffraction separation is required as a first step. We suggest the strategy to use a multiparameter stacking operator, e.g, common-reflection surface, and stack along the midpoint direction. The obtained kinematic wavefield attributes are used to calculate time-migration velocities. A diffractivity map serves as filter to refine the velocities. This strategy is applied to a 3D P-cable data set to obtain a final time-migrated image.

4.2 Introduction

The P-cable technology has been used for years. However, building a reliable velocity-model for 3D time and depth migration is still challenging. The P-cable technology consists of short streamers and a high frequency source. This leads to an increased spatial and lateral resolution with very small bin sizes. The short source-receiver offsets, however, have limitations to determine a velocity model with standard velocity analysis.

The need for a good and appropriate velocity model for time and depth migration is well-known, e.g., a residual move-out (RMO) analysis can be performed to obtain and update a velocity model (see for example Yilmaz (2001)). The method follows an iterative approach based on the analysis of flatness of events after migration. Therefore, the offsets for one specific midpoint are plotted and flatten by updating the velocity model. Another approach, frequently used in processing, is the common-offset migration and the application of inverse normal move-out correction followed by velocity analysis, e.g., Bancroft et al. (1998). These two different methods of velocity-model building have in common, that they require appropriate, i.e., long offsets and a starting velocity model.

P-cable data do not allow model building by conventional methods if an insufficient offset-to-target ratio is present. Diffractions provide a tool for model building even for zero-offset (ZO) data (Bauer et al., 2017). In combination with the high-resolution potential of P-cable data, geological discontinuities, such as, faults, pinch-outs, and small-size scattering objects might be resolved (Klem-Musatov et al., 1994). These features are one of the objectives of seismic interpretation. The seismic response from these features is encoded in diffractions (Khaidukov et al., 2004). A separation of diffracted and reflected energy is mandatory to perform diffraction processing. First applications of diffraction imaging with P-cable data are shown by Merzlikin et al. (2017). They use azimuthal plane-wave destruction to detect faults and channels accounting for different orientations of edge diffractions. Klokov et al. (2017) expand this procedure and apply a 1D diffraction focusing analysis for time migration.

In this paper, we go a step further and perform a consistent velocity-model building based on kinematic wavefield attributes obtained by the common-reflection surface (CRS) method (Müller, 1999). The first step is to separate reflections and diffractions. Furthermore, the diffraction-only data are stacked with a multiparameter stacking method. The byproduct of the stack are the kinematic wavefield attributes. These attributes are used to calculate a 3D velocity model and to perform, e.g., a time migration.

4.3 Method

This part describes the different steps to obtain a migrated time image. We start with the crucial step of separating diffractions from the total wavefield using wavefront attributes. Afterwards, we explain the model-building process and time migration. In all stages, we focus on diffractions because they are the key for the whole process to obtain a migrated image for P-cable data with their short source-receiver offsets.

4.3.1 Separation

There are different possibilities to do the separation of diffractions from the data in time and depth domain. One approach, in depth, is to eliminate focused reflections and demigrate the residual wavefield to obtain diffractions (Moser and Howar, 2008). Mandatory for this approach is an good a prior depth-velocity model. Since we are working in the time domain, another possibility is to use kinematic wavefront attributes for separation, e.g., Dell and Gajewski (2011). A third option is to apply filters designed as finite-difference stencils for the plane-wave differential equation and decompose the seismic records into diffracted and reflected components using plane-waves, e.g., Fomel (2002) and Kozlov et al. (2004). Another method is presented by Schwarz and Gajewski (2017). They calculate the dips and remove them between a user-defined threshold using adaptive subtraction.

We chose the plane-wave destruction method introduced by Claerbout et al. (1992) and Fomel (2002). They state that the seismic image is characterized by a superposition of local plane waves. Then, finite-difference filters are designed to destroy these waves. This procedure is done in two steps: first, estimate the dominant local slope by least-square optimization. Secondly, apply non-stationary plane-wave destruction filters (Fomel, 2002). The remaining data consists the diffractions. This technique can be applied fast without further processing steps and is therefore, favored against the other techniques which require additional processing steps demanding offset information , e.g, the separation with kinematic wavefront attributes. Offset information are valuable for the separation process due to a more stable processing in terms of attribute determination which are used for the accordingly separation method. The separation without appropriate source-receiver offsets is a challenging task and must be performed with great care.

4.3.2 Multiparameter stack

Conventionally stacking is performed along a hyperbola in offset direction. We face the issue that with P-cable data, offsets are very short and fitting hyperbolas is ambiguous. Therefore, we use a multiparameter stacking operator, which stacks the data in midpoint direction, too. There are several operators around, such as, CRS (Müller, 1999; Bergler, 2004), multifocusing (Landa et al., 2010), and non-hyperbolic CRS (Fomel and Kazinnik, 2013). Walda et al. (2017) claim that for complex media the choice of operator to determine wavefront attributes is not important since they provide very similar results. We use the so-called CRS operator to calculate the kinematic wavefront attributes shwon in equation 4.1:

$$t(\mathbf{m}, \mathbf{h}) = (t_0 + \mathbf{p}^T\mathbf{m})^2 + \frac{2t_0}{v_0}\mathbf{m}^T\mathbf{R}\mathbf{K}_N\mathbf{R}^T\mathbf{m} + \frac{2t_0}{v_0}\mathbf{h}^T\mathbf{R}\mathbf{K}_{NIP}\mathbf{R}^T\mathbf{h} \tag{4.1}$$

The coordinates are expressed in terms of midpoint $\mathbf{m}$, half-offset $\mathbf{h}$, and the zero-offset (ZO) travel time t_0. Bold capital letters indicate a 2x2 matrix, and bold small letters are 2D vectors, where the directions correspond to inline and crossline, used in 3D processing. The three additional variables $\mathbf{p}$, $\mathbf{M}$ and $\mathbf{N}$ are the kinematic wavefront attributes (Hubral, 1983). They describe the wavefront and ray geometry (Gelchinsky et al., 1999) and are defined by

$$\mathbf{p} = \frac{-2\sin\alpha}{v_0}\begin{pmatrix}\cos\beta \\ sin\beta\end{pmatrix}, \quad \mathbf{M} = \mathbf{R}\mathbf{K}_{NIP}\mathbf{R}^T, \quad \mathbf{N} = \mathbf{R}\mathbf{K}_N\mathbf{R}^T \tag{4.2}$$

with

$$\mathbf{R} = \mathbf{\Phi}\mathbf{\Theta}, \quad \mathbf{\Phi} = \begin{pmatrix}\cos\beta & -\sin\beta & 0 \\ \sin\beta & \cos\beta & 0 \\ 0 & 0 & 1\end{pmatrix}, \quad \mathbf{\Theta} = \begin{pmatrix}\cos\alpha & 0 & \sin\alpha \\ 0 & 1 & 0 \\ -\sin\alpha & 0 & \cos\alpha\end{pmatrix}. \tag{4.3}$$

Horizontal slowness $\mathbf{p}$ includes the dip angle α and azimuth angle β. The near-surface velocity v_0 is assumed to be known, which is particularly simple in our case since we use marine data in this work. The parameter $\mathbf{R}$ is a rotation matrix to the ray-centered coordinate system. The parameter $\mathbf{N}$ is a two-by-two curvature matrices (see equation **??**) containing the curvature of the normal (N) wave $\mathbf{K}_N$ from a hypothetical wave starting from an exploding reflector segment and emerging at the surface. The parameter $\mathbf{M}$ is a two-by-two matrix containing the curvatures of the normal-incidient point (NIP) wave $\mathbf{K}_{NIP}$ from a hypothetical wave starting from the NIP and emerging at the surface.

Considering ZO, as it is the case for our P-cable data, only two parameters have to be calculated: the slowness $\mathbf{p}$ and curvature matrix of N wave $\mathbf{N}$. For a point diffractor $\mathbf{N} = \mathbf{M}$ is true. We favor the diffraction processing due to the fact that the same information in midpoint and offset direction are available for a point scatterer. In contrast to reflections, where the information are not the same and therefore cannot be used for the special P-cable case, where we deal with ZO data. In conclusion, the ZO CRS operator reduces to shows the ZO CRS operator:

$$t(\mathbf{m}, \mathbf{h} = 0) = (t_0 + \mathbf{p}^T\mathbf{m})^2 + \frac{2t_0}{v_0}\mathbf{m}^T\mathbf{R}\mathbf{K}_N\mathbf{R}^T\mathbf{m} \tag{4.4}$$

4.3.3 Time migration

Normally, offsets are crucial to derive a migration velocity-model.In the absence of this information, we use the wavefront attributes of diffractions to determine a velocity model, which can be used for time migration. Spinner (2006) present a method to calculate the velocity model from the kinematic wavefront attributes using CRS method. She expresses the diffraction CRS operator in apex coordinates and relates the kinematic wavefront attributes with the time-migration velocity

$$\mathbf{V}^2 = (\mathbf{p}\mathbf{p}^T + \frac{2t_0}{v_0}\mathbf{N})^{-1}. \tag{4.5}$$

To further improve the resulting velocity model, we use the approach discussed in Glöckner et al. (2019a). They used a migrated coherence section to weight the velocity model, interpolate gaps and smooth the velocity model. We adopt this approach for the azimuth section and calculate coherence in terms of semblance (Neidell and Taner, 1971) to determine regions with diffractions. This section is weighted with the velocity model to enhance appropriately determined velocities for diffractions. Afterwards, we apply interpolation and smoothing.

The diffraction processing is well suited for a following 3D Kirchhoff time migration, which can be seen as a diffraction operator and is similar to our approach to use diffractions for the P-cable data processing. Because of short P-cable offsets, we can only perform a 3D post stack Kirchhoff time migration.

The next section presents the application of our proposed method to a 3D p-cable data set.

4.4 Application

4.4.1 Data

We have applied this method to a P-cable cube that was recorded by the German research vessel 'Sonne' in late 2016 (Berndt et al., 2016). The cruise investigated the sector collapse of the island Ritter that took place in 1888 to constrain the slide parameters and the tsunami potential of such events. Volcanic island flank collapses have the potential to trigger devastating tsunamis threatening coastal communities and infrastructure (Karstens et al., 2019). Understanding this process is crucial for assessing the hazard potential of volcanoes with slowly deforming flanks like, e.g., Mt Etna and Kilauea.

Ritter Island is a volcanic island located 100 km northeast of New Guinea in the centre of the Bismarck volcanic arc. The present-day morphology is dominated by a horse-shoe shaped scarp formed by the 1888 flank collapse. The uninhabited island is 2 km long, 200 m wide and 140 m high with steep flanks. Prior to the collapse, the island was about 800 m high and had a diameter of 2 km. German colonists documented the generated tsunami, caused by the largest historic flank collapse, and measured run-up heights of 20 m, arrival times, and report damages. These reports are valuable and unique for the estimation of the tsunami potential.

The seismic data are recorded with the 3D P-cable seismic system manufactured by Geometrics. In total sixteen digital streamers were used, four are solid state and twelve are oil-filled. Each streamer had eight hydrophone groups spaced 1.5 m apart and the offset between source and receivers varies between 160 m and 320 m. The source consisted of two GI guns taht were triggered with a shot interval of approximately 10 m (Berndt et al., 2016). The data were pre-processed including the following steps: re-positioning of streamers, 3D binning, frequency filtering (45-240 Hz). Additional processing steps are: a normal move-out correction with water velocity, and stacking.

4.4.2 Results

We illustrate and discuss the different steps of our proposed method exemplary for a part of the acquisition shown in Figure 4.1. This part shows the proximal area of the land slide. The slope of Ritter island and smaller submarine volcanic cones are visible.

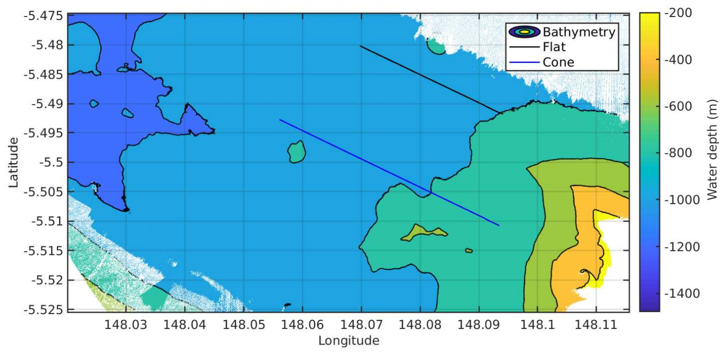

Figure 4.1: Bathymetry of the P-cable data under investigation. Ritter island is located in the Northeast. The two lines show the example crosslines.

We use two different parts of the cube, marked in Figure 4.1, namely a section with a volcanic cone that predates the sector collapse and little sedimentary layering (cone area, blue line), and a section with more sedimentary layering and no cones (flat area, black line). These areas are exemplary used in the further description and visualization of our method, in addition with 3D views of the full data set.

The first step in our work flow is the event separation. Only the assumed point diffractions yield information in midpoint direction, which are necessary to perform a stack and calculate a migration-velocity model. Therefore, a suitable separation is a crucial step to obtain the needed diffraction-only data. Figure 4.2 shows the original data (a) and the separated data after plane- wave destruction (b) for the cone area. Diffractions are better visible after the separation. In addition, reflections in the dipping flank and internal reflections in the middle are reduced. Nevertheless, some artifacts remain, especially for dipping events close to the cone, which should not be considered as pure point diffractions.

Figure 4.3 shows the original data (a) and separated data (b) for the flat area.Here, the plane-wave destruction (PWD) worked better when compared to the cone area, because more sedimentary layering is removed and the diffractions are better visible. Reflections at 1.4 s are well attenuated and show the diffraction energy in the data.

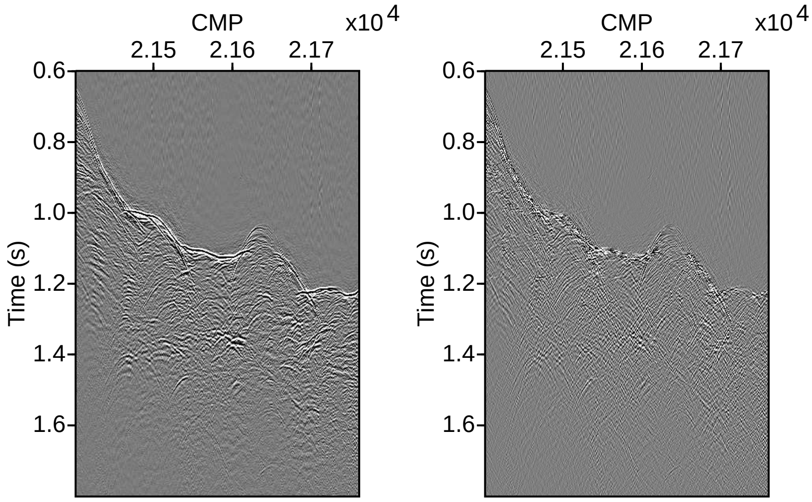

(a) Original data for cone area. (b) Separated data for cone area.

Figure 4.2: Comparison of original and separated data for the area with volcanic cones.

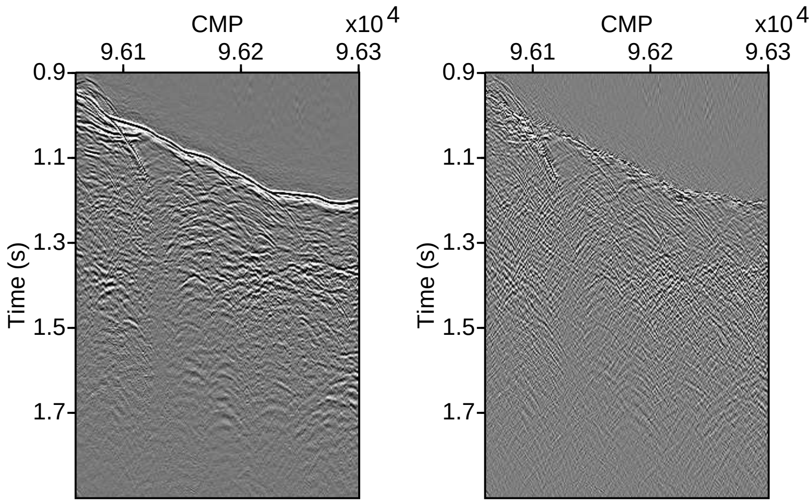

(a) Original data for flat area. (b) Separated data for flat area.

Figure 4.3: Comparison of original and separated data for the area with flat sediments.

The next step is to perform the multiparameter stacking with the diffraction-only data to obtain the stack and coherence sections, as well as, the mentioned kinematic wavefield attributes. Due to the preprocessing offset information are not available, we perform the stack along the midpoint direction. Figure 4.4 shows the stacked sections of the separated diffraction data. The multiparameter stack leads to an improved signal-to-noise ratio and diffractions are better recognizable. Both sections show clear diffraction events in absence of reflections which mask the richness of diffracted wavefield due to higher amplitudes.

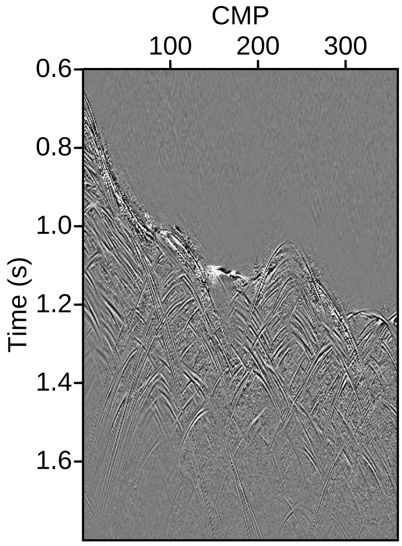

(a) Diffraction stack for cone area.

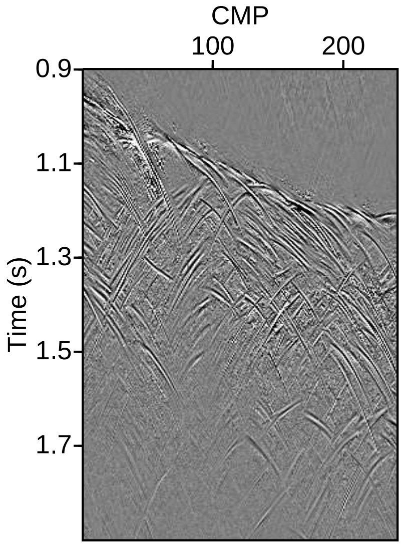

(b) Diffraction stack for flat area.

Figure 4.4: Diffraction stacks for the different example areas showing the diffraction potential of the data.

Figure 4.5 shows a 3D view of the processed P-cable volume. On the right side (east), we see the layered flank of the island. In the middle of the image is a volcanic cone. There, we observe some internal events. The time slice shows circular shaped events which indicate point diffractions. Furthermore, we see that the stack enhances the signal-to-noise ratio in comparison to Figures 4.2 and 4.3.

Another important attribute, the coherence, is shown in Figure 4.6. The cone area (a) as well as the flat area (b) show the diffractions with higher coherence values than the background. One-sided diffraction tails are more visible than full diffraction hyperbolas.

Furthermore, we obtain the kinematic wavefield attributes: the slowness vector and the curvature matrix of the diffracted wave. The attributes are divided in inline and crossline direction. Inline attributes are weaker in terms of quality in comparison to the corresponding crossline attribute due to the special acquisition geometry of P-cable data. We weight our attribute sections with the coherence to simplify the interpretation of the different attribute sections. Therefore, we define a threshold (here 0.1) in the coherence section and use it as weight for the attributes. That means, values of the coherence section above the threshold are multiplied with one, and values below wit zero, respectively. The slowness is divided in dip and azimuth (see Figures 4.7 and 4.8).

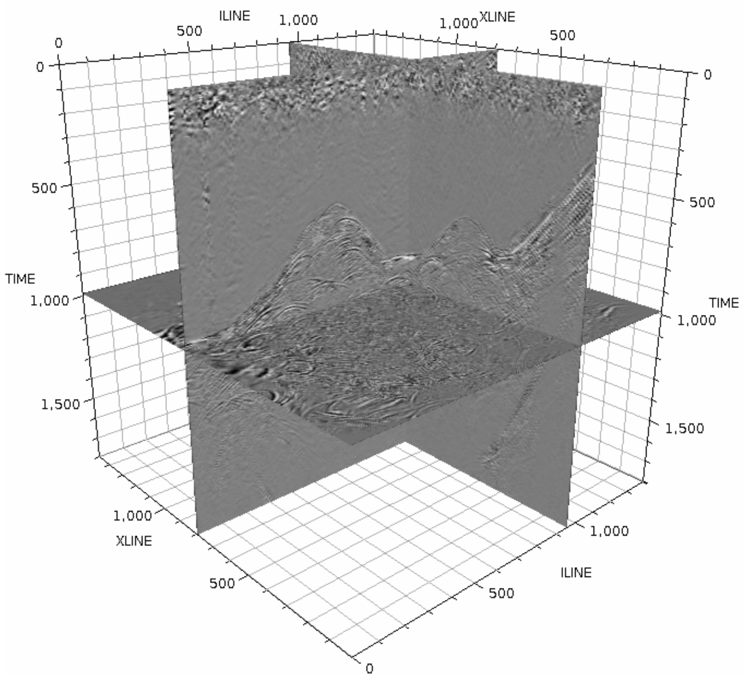

Figure 4.5: Diffraction stack of the processed P-cable data. The viewing direction is from south to north.

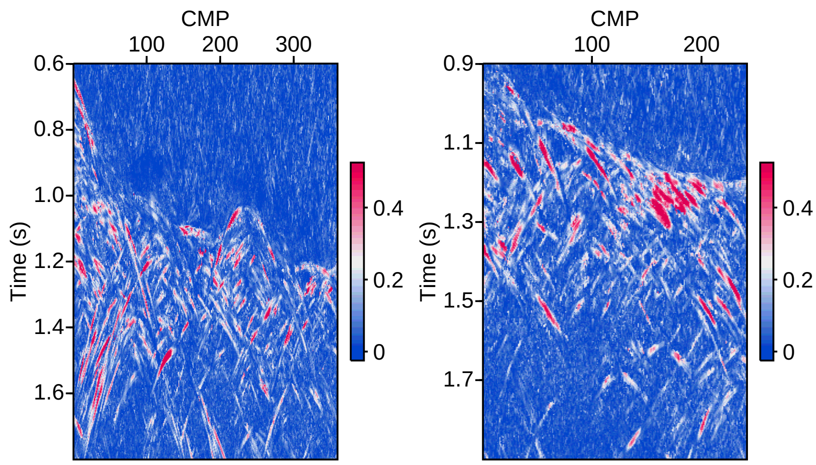

(a) Coherence for cone area. (b) Coherence for flat area.

Figure 4.6: Coherence section for the different example areas.

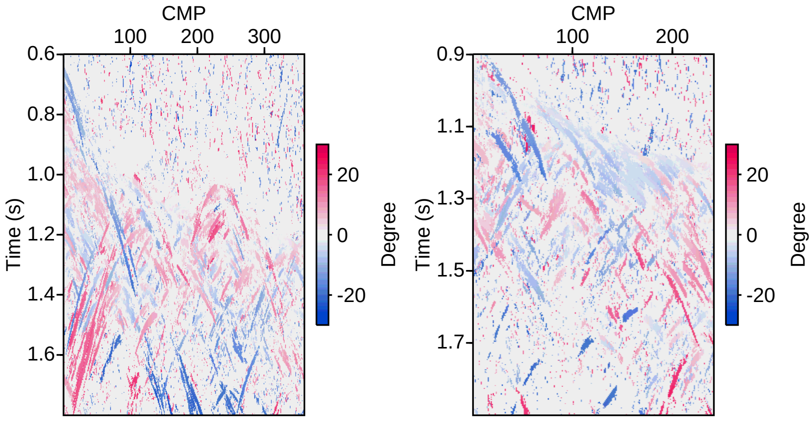

(a) Dip for cone area. (b) Dip for flat area.

Figure 4.7: Dip angle for the different example areas.

Figure 4.7 shows the dip section for the areas under investigation. Dip ranges from -27 to 27 degrees, which is normal when considering diffractions with steep dipping tails. Events are also visible on the basis of dip information. The dip attribute can be used for a quality control of the separation. Here, only few events with dips close to zero are visible. Small dips are usually attributed to indicating reflections. However. the apex region of the diffractions have also dips close to zero, which is better visible in the flat area (b).

Figure 4.8 shows the azimuth section for the areas under investigation. We obtain narrow azimuths due to the acquisition geometry and the special P-cable technology. The azimuth images for the cone area (a) as well as the flat area (b) show many diffraction events.

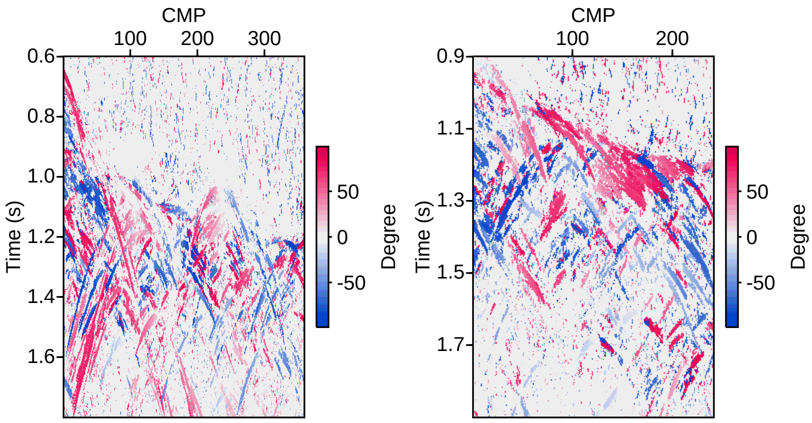

(a) Azimuth for cone area. (b) Azimuth for flat area.

Figure 4.8: Azimuth for the different example areas.

In addition, we obtain the curvature matrix of the diffracted wave, which represents the second order derivatives of travel times in inline and crossline direction, and consists of three independent entries (see Figures 4.9, and 4.10). Figure 4.9 shows the different curvature matrix entries for the cone area and represent inverse curvature radii. The images are not as clean as the dip and azimuth images, due to their second-order derivative nature.

Especially image (a) and (b) show diffractions, which have high curvatures. The values close to the sea bottom are more clean than deeper parts. The attribute N_{01} from the mixed second-order derivative is the most unreliable and noisiest one.

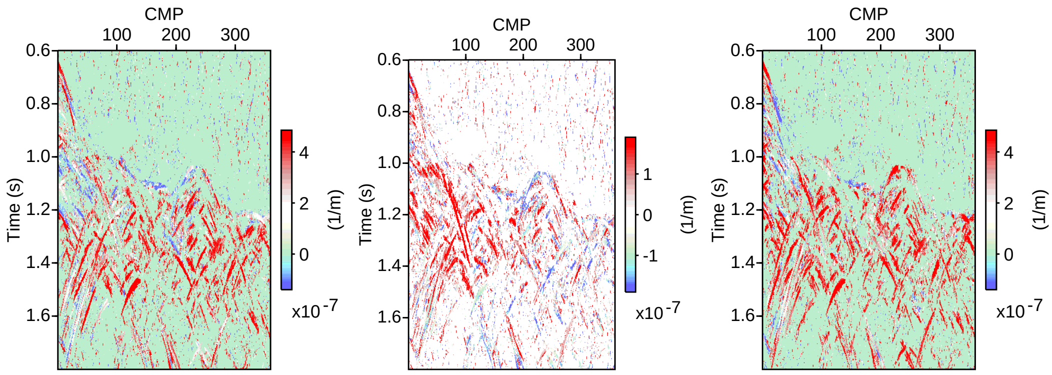

(a) N_{00} for cone area. (b) N_{01} for cone area. (c) N_{11} for cone area.

Figure 4.9: Curvatures of diffraction-only data for the cone area.

Figure 4.10 shows the different curvatures for the area dominated by sedimentary layering. Here, events are better visible in comparison to Figure 4.9. Again, attributes N_{00} (a) and N_{11} (c) show clearer events in comparison with N_{01} (b).

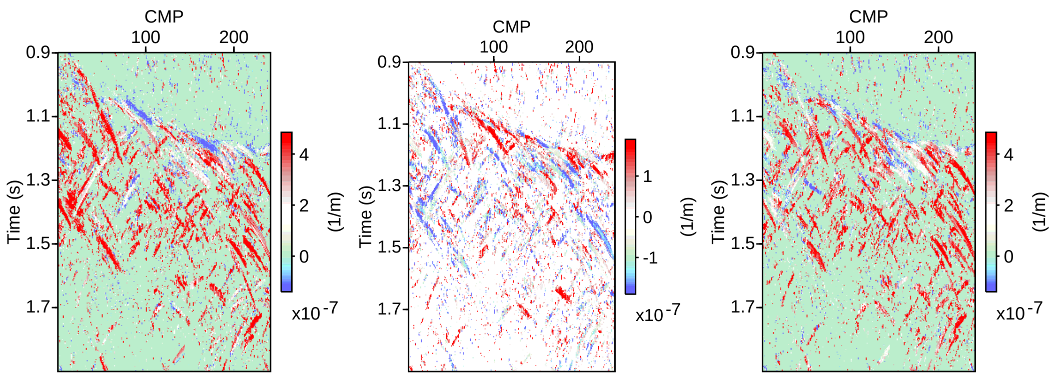

(a) N_{00} for flat area. (b) N_{01} for flat area. (c) N_{11} for flat area.

Figure 4.10: Curvatures of diffraction-only data for area with sedimentary layering.

Now, all attributes needed for velocity-model building are available and time migration can be performed. Figure 4.11 shows the calculated time-migration velocity for both example areas. In general, velocities show appropriate values but some artifacts are visible. Higher velocities (in red) occur close to the ocean bottom for the flat area b) and on the left part for the cone area a). A reason for this is the difficult separation process and the stacking in just the common-midpoint (CMP) direction. The attributes, needed for the calculation of the velocities, are in some areas noisy as well and lead to erroneous velocities. Especially, reflection artifacts from the ocean bottom increase velocities due to insufficient curvature radii.

The migrated images are shown in Figure 4.12. The sea bottom is visible with the typical

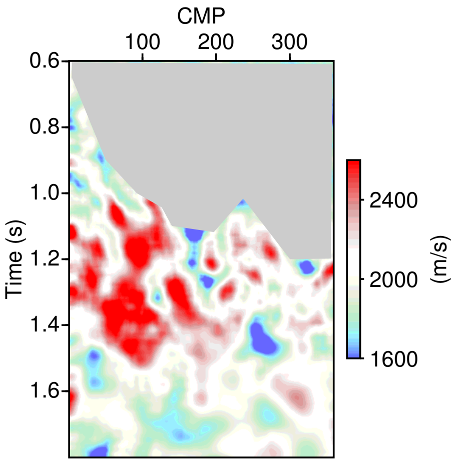

(a) Time-migration velocity for cone area.

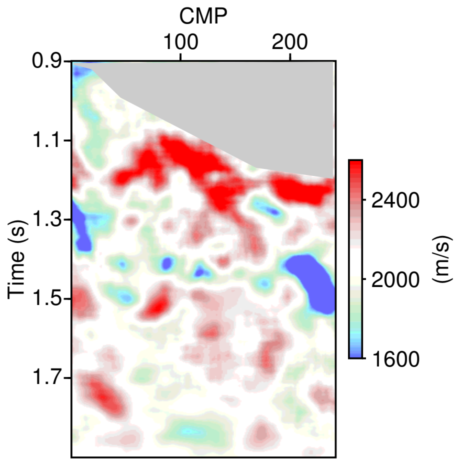

(b) Time-migration velocity for flat area.

Figure 4.11: Time-migration velocities for the different example areas. Smoothing and a mute of the water column (gray) is applied.

time-migration artifacts, which are mainly covered by the mute of the water column. The cone in Figure 4.12 (a) is less prominent than in Figure 4.2 or Figure 4.4 (a). However, we observe further events between 1.2 and 1.4 s. The migrated image for the flat area (b) shows a structure in the middle between 1.1 and 1.3 s. The velocity is less reliable in this area (see Figure 4.11 b) due to high velocity spots in the upper part.

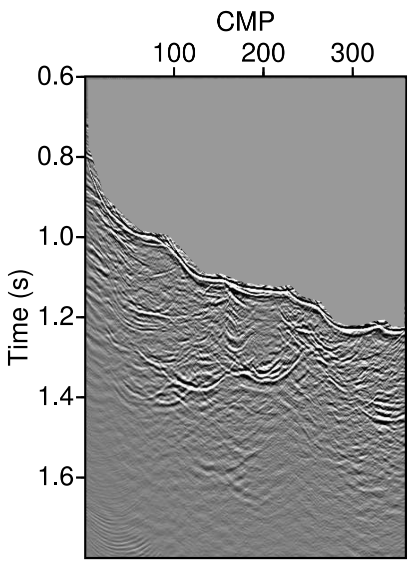

(a) Migrated image for cone area.

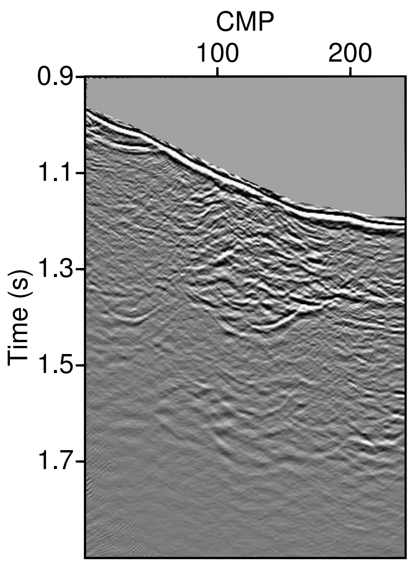

(b) Migrated image for flat area.

Figure 4.12: Time migration results for both example areas. The water column is muted.

Figure 4.13 shows a 3D-view of the migrated P-cable volume and is the same as for Figure 4.5 for comparison. The cone in the migrated image is smaller than in the stacked image. Furthermore, we see sedimentary layering under the ocean bottom. The time slice shows a complex pattern in the south-west related to the diffractions there.

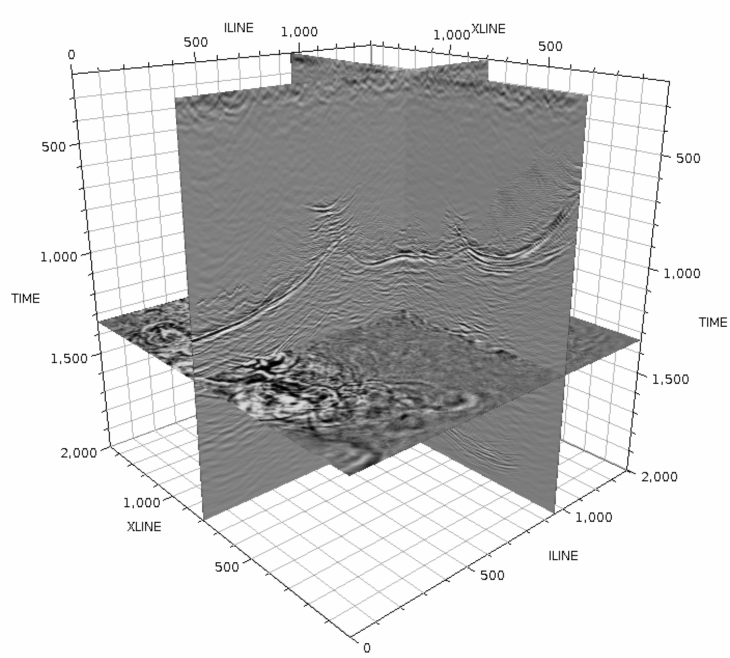

Figure 4.13: Time-migrated image of the processed P-cable data. The viewing direction is from south to north.

The application shows that the proposed approach leads to a time-migrated image. We are able to produce this without any offset information using a work flow designed for diffractions.

4.5 Discussion

In this section, we discuss the advantages, challenges, and issues of the proposed approach to obtain a velocity model and perform a time migration for 3D P-cable data. The short source-receiver offsets from P-cable data make standard velocity analysis almost impossible. The CRS-based diffraction processing with kinematic wavefront attributes for such data sets allows for the determination of a velocity model suitable for time migration. Unfortunately, different preprocessing steps, e.g. interpolation and filter methods, reduce the diffraction energy because they limit or smear over dip ranges. Preprocessing must be performed diffraction-friendly to preserve especially large dip values, which are typical for diffractions.

The assumption that we handle with pure point diffractions offers the possibility to use a multiparameter stacking operator in midpoint direction instead of offset. Because of the weak amplitudes of diffractions, we have to perform a careful diffraction separation. Here, we are using the plane-wave destruction introduced by Fomel (2002). The separation is the crucial point in this approach and has room for improvements as shown in Merzlikin et al. (2017). They apply the plane-wave destruction for different azimuths and achieve improved results. We are not able to apply this procedure due to limited azimuths in our data set.

The time-migration velocities obtained from the kinematic wavefield attribute can be further improved. We must not forget, that for velocity analysis appropriate offset information are crucial. For the P-cable data sets, we are missing this kind of information. Therefore, we just applied a smoothing of time-migration velocities due to a needed smooth velocity distribution for time migration.
The time-migrated images show that our method generally works. We propose a consistent way to achieve a migrated image without additional information, such as ocean-bottom seismometer or long offset 2D surveys.

First attempts to perform velocity-model building for depth migration are done by Glöckner et al. (2018) and Glöckner et al. (2019d). They use the kinematic wavefield attributes as input for the wavefront tomography (Duveneck, 2004; Klüver, 2007). The wavefront tomography consists of two parts: the picker and the inversion. The automatic picker chooses samples with a user-defined coherence value and the corresponding kinematic wavefield attributes. These values are used for the inversion to calculate a depth-velocity model. Glöckner et al. (2019d) show that it is crucial to eliminate as much non-point-diffraction energy as possible. Reflection artifacts boost velocities and lead to overestimated velocity models which are not yet suitable for a depth migration. Furthermore, the second-order curvature attributes are less reliable then the first-order slowness attributes. They are more stable, when having appropriate source-receiver offset for the calculation. Bauer et al. (2019) show an approach for the wavefront tomography without the critical second-order curvatures. They use a diffraction focusing criterion for the inversion process. The separation is the most important part for a successful application. This issue must be addressed in future research to obtain improved velocity models for time and depth migration.

4.6 Conclusions

The advantage of P-cable technology is the increased spatial and lateral resolution when compared to conventional 3D data. The short source-receiver offsets prevent standard velocity analysis. We suggest an approach, which can fill this gap, focusing on the diffracted wavefield using the CRS operator. We first perform the separation of diffractions from the total wavefield using plane-wave destruction followed by a multiparameter stack on the diffraction data. Further outputs of the stacking are the kinematic wavefield attributes. These attributes allows us to calculate a velocity model for time migration. The proposed method is applied to a 3D P-cable data set from the Bismarck Sea. The data application shows the challenges when processing data without offset information. Diffractions are the tool to process such data sets which have the potential for time and depth velocity-model building.

5 Conclusions

Time imaging covers a lot of techniques still widely used in industry and academics to obtain an image in time of the subsurface. The developed migration and demigration methods are based on the implicit CRS and provide the basis for the investigated techniques, denoising and migration velocity analysis.

The first and second presented publications (Glöckner et al., 2019a,b) cover the aspect of denoising images. Here, I investigated three techniques, which can all be used to reduce the noise level. The different techniques have different behaviours concerning the kind of noise they suppress. Denoising with demigration mainly regularizes the data. Furthermore, random noise is suppressed by a coherent placement of amplitudes along the demigration operator. To obtain a denoised image a sequence of migration, demigration and remigration must be performed. The migration/demigration loop is also the basis for denoising by migration deconvolution. Here, filters are calculated and convolved with the migrated image to obtain an improved resolution. The field data application shows the strength of the migration deconvolution: it reduces migration swings and recovers amplitudes. The third presented denoising techniques makes use of machine learning algorithms, specifically a deep convolutional neuronal network. The used supervised autoencoder calculates a function which is able to denoise the migrated data after a certain amount of training. With this technique migration noise can be reduced, as well as migration smiles and random noise. The denoising techniques were applied to the same land data set, which contains a salt body and a very complex geology. The final migrated images clearly show an improvement and significant noise reduction in the different described features.

The second aspect of time imaging under investigation is the migration velocity analysis. The first publication (Glöckner et al., 2019a) introduces a detailed time-migration-velocity calculation based on the kinematic wavefield attributes. Furthermore, a refinement for these velocities is presented. Here, I use the coherence section of the migrated image as a filter mask to highlight areas with appropriate migration velocities indicated by higher coherence values. These areas are connected by a subsequent interpolation and smoothing. The presented migration velocity analysis is data-driven and executable in an automated fashion. Minimal user interaction is required to define a threshold for the coherence filter. The resulting migrated image has an improved resolution in comparison with an image obtained without the suggested refinement. The improved migrated images are used for all presented denoising techniques. A modified migration velocity analysis is used for the refinement of the P-cable data. There, I use the coherence section of a diffractivity image, which shows where focused diffractions are located, as a filter for the subsequent refinement to improve the migrated image.

The third publication (Glöckner et al., 2019c) shows the application of some of the investigated time processing methods to challenging 3D P-cable data. The special characteristics of P-cable are the short source-receiver offset and a high-frequency content. These features lead to an improved resolution of the data in comparison with conventional 3D data acquisition but make the velocity-model building very challenging. Usually a full source-receiver offset coverage is required to calculate an appropriate velocity model. Since this is not available for P-cable data, I present a diffraction-based approach, which is able to stack the data and calculate time-migration velocities based on the kinematic wavefield attributes in 3D. The velocities are refined with a diffractivity map and used for a 3D Kirchhoff time migration.

All investigated techniques improve the migrated image. Especially, the denoising has a lot of potential to improve the quality of low fold land data. The migration velocity refinement is an indispensable step to obtain an enhanced migrated image and is used for all denoising techniques under investigation. All techniques depend on the implicit CRS-based migration/demigration algorithm.

6 Outlook

The ideas and results presented in this thesis are intermediate steps and part of on-going research. Therefore, I see the potential for several possible future topics related to my work.

6.1 Migration and demigration

The time migration and demigration is so far formulated in 2D. A 3D extension is desirable to apply the denoising work flows, i.e., demigration, migration deconvolution, and the autoencoder, to 3D data. Especially P-cable data could benefit from the advantages of the presented denoising methods. The demigration followed by a subsequent remigration is the basis for these methods. For the 3D case, the number of kinematic wavefield attributes increases from three to eight attributes. Therefore, relations should be accurately investigated. First attempts are presented by Bergler (2004).

6.2 Machine learning

Another aspect is the transfer learning ability of the used deep convolutional neuronal network, i.e the application to other data sets with a similar geology as the trained one with complex salt structures. The analysis of the denoising results will give a hint about the generalization and usability of the trained network for other data sets with similar geology. Machine learning algorithms can be further expanded. I think about testing different network architectures or performing the training in an unsupervised fashion. Another idea is to perform migration with machine learning algorithms. The migrated image could be used as a target to train a network that maps prestack data into migrated images.

6.3 P-cable data

Writing my thesis research, I applied different processing work flows to P-cable data not presented in the papers here. For instance I investigated the velocity-model building in depth (Glöckner et al., 2018, 2019d). To emphasize the topic and issues in depth, I summarize the conference paper by Glöckner et al. (2019d).

The work flow is the same as described in chapter 4. Separation and stacking of the P-cable data is performed to obtain the kinematic wavefield attributes. These attributes (dip angle and curvature of **M** wave) serve now as input for the wavefront tomography (Duveneck, 2004; Klüver, 2007). Due to the assumption of point scattering, I am only able to calculate

the **N** wave curvatures. For real diffractions count $\mathbf{M} = \mathbf{N}$. Since, I am calculating the **N** wave curvature due to missing offsets, inaccuracies occur. Further artifacts results from the assumption of point diffractions, the diffraction separation, and noise and lead to erroneous picks. These picks result in high and unrealistic depth velocities after the inversion. I introduce the cluster algorithm k-means (e.g. MacQueen et al., 1967) as quality control for the erroneous picks and apply it before the inversion in an iterative fashion. The cluster algorithm partitions the picks in different clusters. Then, non-diffraction cluster are sorted out by investigating the different subsets of wavefield attributes. After the reduction and deletion of erroneous picks, I use the remaining picks for the inversion part.
Figure 6.1 shows the improvement obtained with the cluster algorithm. The velocities are reduced by a maximum of 1000 m/s with the suggested quality control by a machine learning algortihm.

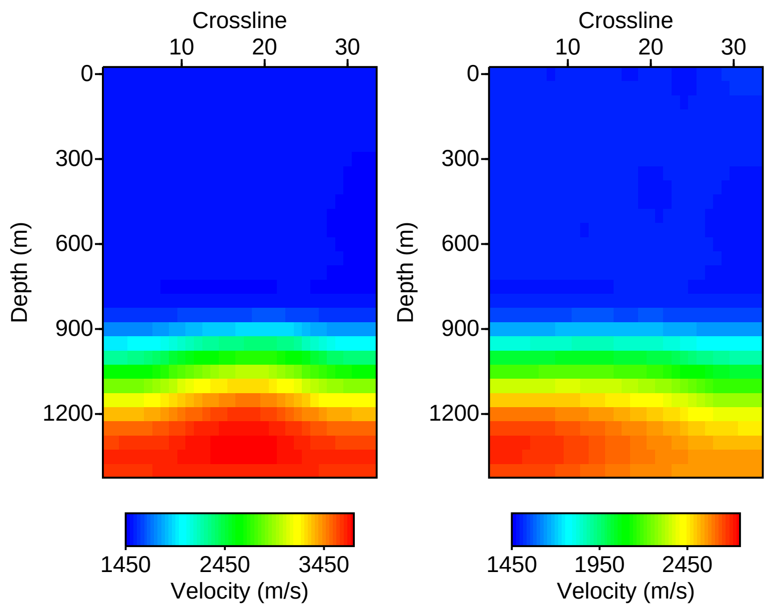

Figure 6.1: Final velocity model, without ML (left), using suggested ML algorithm (right). Please note the different legends (Glöckner et al., 2019d).

Figure 6.2 shows the obtained velocity values from the tomography with and without clustering as well as the velocity profile calculated from ocean-bottom seismometer (OBS) data. The OBS profile has the most realistic and lowest velocities in comparison with the inversion. The disadvantage is the selective 1D velocity model from OBS measurements. The proposed cluster method performs better, in terms of lower velocities, than the original inversion with erroneous picks. Nevertheless, the low-velocity anomaly between 1100 m and 1200 m cannot be detected with the tomography. Reasons for this can be the resolution of the tomography or a lack of diffractions at this depth.

The results of the presented approach are promising, but the obtained depth-velocity model requires further verification. Depth models must be more precise in comparison with velocity models for time migration. Strategies should be formulated to steer the velocity-model building so that it is suitable for a subsequent depth migration. One approach is to improve the necessary separation of reflections and diffractions. Reflection artifacts and other leftovers, e.g. noise, increase the velocities during the wavefront tomography. Here,

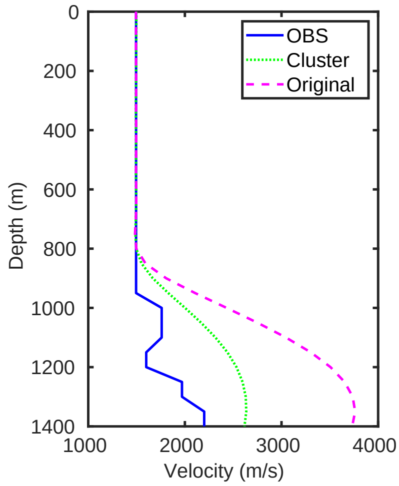

Figure 6.2: Velocity model from OBS measurement and inversion results with and without clustering.

I am working on an approach where machine learning is used for the separation. The aim is to develop and train a network to be able to separate reflections and diffractions more precisely than the presented methods. Since diffractions are naturally 3D effects, a trained network for this case could improve the separation result and the subsequent processing. Another step concerning the inversion is the focusing criterion for diffractions during the wavefront tomography. I used a focusing criterion of diffractions for building time-migration velocities. The criterion implies that the correct velocity provides the highest semblance for the focused diffraction. A similar or another focusing criterion (Bauer et al., 2019b; Znak et al., 2018) could also be used for wavefront tomography. Another potential improvement is changing the input data for the tomography. The first-order attributes are very stable in contrast to the second-order attributes. Using only the first-order attributes or a reweighting of the input data in correspondence with reliability of the attributes can provide an improvement in velocity-model building in depth.

List of Publications

Journal papers

- Glöckner, M., Dell, S., Schwarz, B, Vanelle, C. and Gajewski, D. (2019), 'Velocity-estimation improvements and migration/demigration using the common-reflection surface with continuing deconvolution in the time domain', *Geophysics*, 84(4), p. S229-S238
- Glöckner, M., Walda, J. ,Dell, S., and Gajewski, D. (2019), 'Denoising migrated data with a deep neuronal network', *Geophysics*, submitted
- Glöckner, M., Walda, J. ,Dell, S., Gajewski, D., Karstens, J., Kläschen, D. and Berndt, C. (2019),'Imaging zero-offset 3D P-cable data with CRS method', *Geophysical Journal International*, accepted

Expanded abstracts

- Bobsin, M., Schwarz, B, Vanelle, C. and Gajewski, D. (2015), 'Data-driven time migration using a multiparameter approach', in: Expanded Abstracts, SEG, pp. 4350-4354
- Bobsin, M., Schwarz, B, Vanelle, C. and Gajewski, D. (2015), 'Time migration applying the i-CRS operator', in: Expanded Abstracts, DGG, p. 125
- Glöckner, M., Schwarz, B, Vanelle, C. and Gajewski, D. (2016), 'Kinematic time demigration with an automatically generated velocity model', in: Expanded Abstracts, EAGE
- Glöckner, M., Gajewski, D., Kläschen, D., Muff, S. and Berndt, C. (2018), 'Wavefront tomography with diffraction-only 3D P-cable data', in: Expanded Abstracts, SEG, pp. 5133-5136
- Glöckner, M., Gajewski, D., Kläschen, D., and Berndt, C. (2019), 'Velocity-model building with 3D P-cable data', in: Expanded Abstracts, DGG, p. 141
- Glöckner, M., Walda, J., Gajewski, D., Roth, T., and Berndt, C. (2019), 'Challenges in velocity-model building with 3D P-cable data', in: Expanded Abstracts, EAGE

Bibliography

Abadi, M., Barham, P., Chen, J., Chen, Z., Davis, A., Dean, J., Devin, M., Ghemawat, S., Irving, G., Isard, M. et al. (2016), Tensorflow: a system for large-scale machine learning., *in* 'OSDI', Vol. 16, pp. 265–283.

Agostinelli, F., Anderson, M. R. and Lee, H. (2013), 'Adaptive Multi-Column Deep Neural Networks with Application to Robust Image Denoising', *Advances in Neural Information Processing Systems* pp. 1493–1501.

Arganda-Carreras, I., Turaga, S., Berger, D., Ciresan, D., Giusti, A., Gambardella, L., Schmidhuber, J., Laptev, D., Dwivedi, S., Buhmann, J., Liu, T., Seyedhosseini, M., Tasdizen, T., Kamentsky, L., Burget, R., Uher, V., Tan, X., Sun, C., Pham, T., Bas, E., Uzunbas, M. and Cardona, A.and Schindelin, J. S. H. (2015), 'Crowdsourcing the creation of image segmentation algorithms for connectomics', *Frontiers in Neuroanatomy* **9**(142), 1–13.

Bancroft, J. C., Geiger, H. D. and Margrave, G. F. (1998), 'The equivalent offset method of prestack time migration', *Geophysics* **63**(6), 2042–2053.

Bauer, A., Diekmann, L. and Gajewski, D. (2019), Wavefront Tomography with Enforced Diffraction Focusing, *in* 'Expanded Abstracts', EAGE.

Bauer, A., Schwarz, B. and Gajewski, D. (2017), 'Utilizing diffractions in wavefront tomography', *Geophysics* **82**(2), R65–R73.

Bauer, A., Schwarz, B., Werner, T. and Gajewski, D. (2019b), 'Unsupervised event identification and tagging for diffraction focusing', *Geophysical Journal International* **217**(3), 2165–2176.

Baykulov, M., Brink, H. J., Gajewski, D. and Yoon, M. K. (2009), 'Revisiting the structural setting of the Glueckstadt Graben salt stock family, North German Basin', *Tectonophysics* **470**(1-2), 162–172.

Baykulov, M. and Gajewski, D. (2009), 'Prestack seismic data enhancement with partial common-reflection-surface (crs) stack', *Geophysics* **74**(3), V49–V58.

Beckouche, S. and Ma, J. (2014), 'Simultaneous dictionary learning and denoising for seismic data', *Geophysics* **79**(3), A27–A31.

Bergler, S. (2004), On the determination and use of kinematic wavefield attributes for 3D seismic imaging, PhD thesis, University of Karlsruhe.

Berndt, C., Muff, S., Klaucke, I., Watt, S., Böttner, C., Schramm, B., Völsch, A.-M., Bennecke, S., Elger, J., Chi, W.-C., Van Haren, J., Micallef, A. and Roth, T. (2016), RV SONNE 252 Cruise Report: Tsunami potential of volcanic flank collapses, Technical report.

Bleistein, N., Cohen, J. and Stockwell Jr., J. (2001), *Mathematics of Multidimensional Seismic Imaging, Migration, and Inversion*, Springer Verlag, New York.

Bonar, D. and Sacchi, M. (2012), 'Denoising seismic data using the nonlocal means algorithm', *Geophysics* **77**(1), A5–A8.

Canales, L. L. (1984), *Random noise reduction*, Society of Exploration Geophysicists, Atlanta.

Claerbout, J. F. (1970), 'Coarse Grid Calculations of Waves in Inhomogeneous Media With Application to Delineation of Complicated Seismic Structure', *Geophysics* **35**(3), 407–418.

Claerbout, J. F., Karrenbach, M. and Balog, O. (1992), *Earth Soundings Analysis: Processing versus Inversion*, Blackwell Sci. Publ. Inc.

Claerbout, J., Green, C. and Green, I. (1996), *Imaging the Earth's Interior*, Free Software Foundation.

Dell, S. and Gajewski, D. (2011), 'Common-reflection-surface-based workflow for diffraction imaging', *Geophysics* **76**, S187–S195.

Dell, S., Vanelle, C. and Gajewski, D. (2012), 'Prestack time migration by common-migrated-reflector-element stacking', *Geophysics* **77**(3), S73–S82.

Di, H., Wang, Z. and AlRegib, G. (2018), Deep convolutional neural networks for seismic salt-body delineation, *in* 'AAPG Annual Convention and Exhibition'.

Dice, L. R. (1945), 'Measures of the amount of ecologic association between species', *Ecology* **26**(3), 297–302.

Duveneck, E. (2004), Tomographic determination of seismic velocity models with kinematic wavefield attributes, PhD thesis, University of Karlsruhe.

Fomel, S. (2002), 'Applications of plane-wave destruction filters', *Geophysics* **67**(6), S139–S147.

Fomel, S. (2003), 'Time-migration veloctiy analysis by velocity continuation', *Geophysics* **68**, 1662–1672.

Fomel, S. and Kazinnik, R. (2013), 'Non-hyperbolic common reflection surface stack', *Geophysical Prospecting* **61**, 21–27.

Fowler, P. (1985), Migration Velocity Analysis by Optimization: Linear Theory, *in* 'Expanded Abstracts', Soc. of Expl. Geophys., pp. 660–662.

Gardner, G., French, W. and Matzuk, T. (1974), 'Elements of migration and velocity analysis', *Geophysics* **39**(6), 811–825.

Gelchinsky, B., Berkovitch, A. and Keydar, S. (1999), 'Multifocusing homeomorphic imaging Part 1. Basic concepts and formulas', *Journal of Applied Geophysics* **42**, 229–242.

Glöckner, M., Dell, S., Schwarz, B., Vanelle, C. and Gajewski, D. (2019a), 'Velocity-estimation improvements and migration/demigration using the common-reflection surface with continuing deconvolution in the time domain', *Geophysics* **84**, S229–S238.

Glöckner, M., Gajewski, D., Kläschen, D., Muff, S. and Berndt, C. (2018), Wavefront tomography with difraction-only 3D P-cable data, *in* 'Expanded Abstracts', Soc. of Expl. Geophys., pp. 5133–5136.

Glöckner, M., Schwarz, B., Vanelle, C. and Gajewski, D. (2016), Kinematic time demigration with an automatically generated velocity model, *in* 'Expanded Abstracts', EAGE.

Glöckner, M., Walda, J., Dell, S. and Gajewski, D. (2019b), 'Denoising migrated data with a deep neuronal network', *Geophysics* **submitted**.

Glöckner, M., Walda, J., Dell, S., Gajewski, D., Karstens, J., Kläschen, D. and Berndt, C. (2019c), 'Imaging zero-offset 3D P-cable data with CRS method', *Geophysical Journal International* **accepted**.

Glöckner, M., Walda, J., Gajewski, D., Roth, T. and Berndt, C. (2019d), Challenges in velocity-model building with 3D P-cable data, *in* 'Expanded Abstracts', EAGE.

Goodfellow, I., Bengio, Y. and Courville, A. (2016), *Deep Learning*, MIT Press.
URL: *http://www.deeplearningbook.org*

Guitton, A. (2004), 'Amplitude and kinematic corrections of migrated images for nonunitary imaging operators', *Geophysics* **69**(4), 1017–1024.

Hagedoorn, J. (1954), 'A process of seismic reflection interpretation', *Geophysical Prospecting* **2**, 85–127.

Hertweck, T., Jäger, C., Goertz, A. and Schleicher, J. (2003), 'Aperture effects in 2.5D Kirchhoff migration: A geometrical explanation', *Geophysics* **68**, 1673–1684.

Hu, J., Schuster, G. T. and Valasek, P. (2001), 'Poststack migration deconvolution', *Geophysics* **66**, 939–952.

Hubral, P. (1983), 'Computing true amplitude reflections in a laterally inhomogeneous earth', *Geophysics* **48**, 1051–1062.

Hubral, P., Schleicher, J. and Tygel, M. (1996), 'A unified approach to 3-D seismic reflection imaging, Part I: Basic concepts', *Geophysics* **61**(3), 742–758.

Hübscher, C. and Netzeband, G. (2007), 'Evolution of a young salt giant: The example of the Messinian evaporites in the Levantine Basin.', *In: Wallner, M., Lux, K.-H., Minkley, W., Hardy, Jr., H.R. (Eds.) The Mechanical behaviour of Salt - Understanding of THMC Processes in Salt* pp. 175–184.

Huygens, C. (1690), *Traite de la Lumiere*, Van der Aa, Leyden.

Iversen, E., Tygel, M., Ursin, B. and de Hoop, M. (2012), 'Kinematic time migration and demigration of reflections in pre-stack seismic data', *Geophysical Journal International* **189**, 1635–1666.

Jäger, R., Mann, J., Höcht, G. and Hubral, P. (2001), 'Common-reflection-surface stack: Image and attributes', *Geophysics* **66**, 97–109.

Ji, J. (1994), 'Toward an exact adjoint: Semicircle versus hyperbola', *Stanford Exploration Project* **SEP-80**, 499–512.

Karstens, J., Berndt, C., Urlaub, M., Watt, S. F., Micallef, A., Ray, M., Day, S. J., Klaucke, I., Kühn, M., Muff, S., Klaeschen, D., Böttner, C., Schramm, B., Elger, J., Roth, T. and Brune, S. (2019), 'From gradual spreading to catastrophic collapse - 3D seismic reconstruction of the 1888 Ritter Island volcanic sector collapse', *Journal of Earth and Planetary Science* **517**, 1–13.

Khaidukov, V., Landa, E. and Moser, T. J. (2004), 'Diffraction imaging by focusing-defocusing: An outlook on seismic superresolution', *Geophysics* **69**(10), 1478–1490.

Klem-Musatov, K., Hron, F. and Lines, L. (1994), *Theory of Seismic Diffractions*, Society of Exploration Geophysicists.

Klokov, A., Trevino, R. H. and Meckel, T. A. (2017), 'Diffraction imaging for seal evaluation using ultra high resolution 3D seismic data', *Marine and Petroleum Geology* **82**, 85–96.

Klüver, T. (2007), Velocity model building using analytic and model-based diffraction traveltime functions, PhD thesis, University of Karlsruhe.

Kozlov, E., Barasky, N., Korolev, E., Antonenko, A. P. and Koshchuk, E. (2004), Imaging scattering objects masked by specular reflections, *in* 'Expanded Abstracts', Soc. of Expl. Geophys., pp. 1131–1134.

Lambaré, G., Virieux, J., Madariaga, R. and Jin, S. (1992), 'Iterative asymptotic inversion in the acoustic approximation', *Geophysics* **57**, 1138–1154.

Landa, E., Keydar, S. and Moser, T. J. (2010), 'Multifocusing revisited - inhomogeneous media and curved interfaces', *Geophysical Prospecting* **58**, 925–938.

MacQueen, J. et al. (1967), Some methods for classification and analysis of multivariate observations, *in* 'Proceedings of the fifth Berkeley symposium on mathematical statistics and probability', Vol. 1, Oakland, CA, USA, pp. 281–297.

Merzlikin, D., Meckel, T. A., Fomel, S. and Sripanich, Y. (2017), 'Diffraction imaging of high-resolution 3D P-cable data from the Gulf of Mexico using azimuthal plane-wave destruction', *FirstBreak* **35**, 35–41.

Moser, T. and Howar, C. (2008), 'Diffraction imaging in depth', *Geophysical Prospecting* **56**, 627–641.

Müller, T. (1999), Seismic imaging without explicit knowledge of the velocity model, PhD thesis, University of Karlsruhe.

Neidell, N. and Taner, T. M. (1971), 'Semblance and other coherency measures for multichannel data', *Geophysics* **36**, 482–497.

Nelder, J. and Mead, R. (1965), 'A simplex method for function minimization', *Computer Journal* **7**, 308–313.

Nemeth, T., Wu, C. and Schuster, G. T. (1999), 'Least-squares migration of incomplete reflection data', *Geophysics* **64**, 208–221.

Netzeband, G., Gohl, K., Hübscher, C., Ben-Avraham, Z., Dehgahni, A., Gajewski, D. and Liersch, P. (2006), 'The Levantine Basin - crustal structure and origin Messinian evaporites in the Levantine Basin', *Tectonophysics* **418**, 178–188.

Paffenholz, J., Stefani, J., Mclain, B. and Bishop, K. (2002), Sigsbee2a Synthetic Subsalt Dataset - Image Quality as Function of Migration Algorithm and Velocity Model Error, *in* 'Expanded Abstracts', EAGE.

Powers, D. M. (2011), 'Evaluation: from precision, recall and f-measure to roc, informedness, markedness and correlation', *Journal of Machine Learning Technologies* **2**(1), 37–63.

Ronneberger, O., Fischer, P. and Brox, T. (2015), U-net: Convolutional networks for biomedical image segmentation, *in* 'International Conference on Medical image computing and computer-assisted intervention', Springer, pp. 234–241.

Schleicher, J., Costa, J. and Novais, A. (2008), 'Time-migration velocity analysis by image-wave propagation of common-image gathers', *Geophyiscs* **73**, 161–171.

Schneider, W. (1978), 'Integral formulation for migration in two and three dimensions', *Geophysics* **43**, 49–76.

Schuster, G. (1993), Least-squares crosswell migration, *in* 'Expanded Abstracts', Soc. of Expl. Geophys., p. 110–113.

Schwarz, B. (2011), A new nonhyperbolic multi-parameter operator, Master's thesis, University of Hamburg.

Schwarz, B. and Gajewski, D. (2017), 'Accesing the diffracted wavefield by coherent subtraction', *Geophysical Journal International* **211**, 45–49.

Schwarz, B., Vanelle, C., Gajewski, D. and Kashtan, B. (2014), 'Curvatures and inhomogeneities: An improved common-reflection-surface approach', *Geophysics* **79**(5), S231–S240.

Sheriff, R. and Geldart, L. (1995), *Exploration Seismology*, Cambridge University Press, New York.

Shi, Y., Wu, X. and Fomel, S. (2018), Automatic salt-body classification using a deep convolutional neural network, *in* 'SEG Technical Program Expanded Abstracts 2018', Society of Exploration Geophysicists, pp. 1971–1975.

Shurtleff, R. N. (1984), An f-k procedure for prestack migration and migration velocity analysis, *in* 'Expanded Abstracts', EAGE.

Sorensen, T. A. (1948), 'A method of establishing groups of equal amplitude in plant sociology based on similarity of species content and its application to analyses of the vegetation on danish commons', *Biol. Skar.* **5**, 1–34.

Spinner, M. (2006), 3D CRS-based limited aperture Kirchhoff time migration, *in* 'Expanded Abstracts', Soc. of Expl. Geophys., pp. 2354–2358.

Spinner, M. (2007), CRS-based minimum-aperture Kirchhoff migration in the time domain, PhD thesis, University of Karlsruhe.

Treitel, S. (1974), 'The Complex Wiener Filter', *Geophysics* **39**(2), 169–173.

Tygel, M., Schleichert, J. and Hubral, P. (1996), 'A unified approach to 3-D seismic reflection imaging , Part II : Theory', **61**(3), 759–775.

Vanelle, C., Kashtan, B., Dell, S. and Gajewski, D. (2010), A new stacking operator for curved subsurface structures, *in* 'Expanded Abstracts', Soc. of Expl. Geophys., pp. 3609–3613.

Vincent, P., Larochelle, H., Lajoie, I., Bengio, Y. and Manzagol, P.-A. (2010), 'Stacked Denoising Autoencoders: Learning Useful Representations in a Deep Network with a Local Denoising Criterion', *Journal of Machine Learning Research* **11**, 3371–3408.

Walda, J., Schwarz, B. and Gajewski, D. (2017), 'A competitive comparison of multiparameter stacking operators', *Geophysics* **82**(4), V275–V283.

Wang, Z., Di, H., Shafiq, M. A., Alaudah, Y. and AlRegib, G. (2018), 'Successful leveraging of image processing and machine learning in seismic structural interpretation: A review', *The Leadin Edge* **37**.

Yilmaz, O. (2001), *Seismic Data Analysis*, SEG, Tulsa.

Yilmaz, O. and Chambers, R. (1984), 'Migration velocity analysis by wave-filed extrapolation', *Geophysics* **49**(10), 1664–1674.

Yilmaz, O. and Claerbout, J. F. (1980), 'Prestack partial migration', *Geophysics* **45**, 1753–1779.

Zhu, J., Lines, L. and Gray, S. (1998), 'Smiles and frown in migration/velocity analysis', *Geophysics* **63**(4), 1200–1209.

Znak, P., Kashtan, B. and Gajewski, D. (2018), Velocity model building by geometrical spreading focusing, *in* 'Expanded Abstracts', Soc. of Expl. Geophys., pp. 5188–5192.

Danksagung

Es gibt viele Personen in meinem Umfeld, die zum Gelingen der Promotion beigetragen haben. Als erstes möchte ich meinem Ehemann Robert Glöckner danken. Er hat mich all die Jahre in beruflichen und privaten Angelegenheiten unterstützt. Insbesondere in den letzten Jahren bei der Betreuung unserer Tochter hat er eine tolle Arbeit geleistet. Desweitern möchte ich meinem Kollegen Jan Walda danken. Ohne ihn hätte ich die Promotion vielleicht abgebrochen. Er hat mir neue Perspektiven gezeigt und die Unterstützung gegeben diese auch umzusetzen. Ohne ihn gäbe es keine Kaffepause und viele Gespräche über verschiedenste Themen wären nicht geführt worden. Auch Sergius Dell hat mir mit seinem Wissen und gemeinsamen Gesprächen sehr geholfen den Überblick zu bewahren und meine Arbeit richtig einzuordnen. Auch möchte ich meinen Betreuern Dirk Gajewski und Claudia Vanelle danken für die Unterstützung, kritische Zusammenarbeit und vielen Tipps, die mich als Wissenschaftlerin besser gemacht haben. Besonders schätze ich ihre Unterstützung seit ich meine Tochter habe, sodass es mir möglich ist Kindererziehung und Promotion gleichzeitig zu schaffen. Für eine positive Stimmung haben meine Kollegen Dirk Becker, Christain Hübscher, Joachim Bülow, Paola dal Corso und Frauke Grawe beim Mittagessen gesorgt. Die Sponsoren des Wave Inversion Consortium machten diese Arbeit mit der finanziellen Unterstützung erst möglich. Auch möchte ich Christian Hübscher, Richard Blender und Thomas Pohlmann danken, dass sie meiner Prüfungskommission angehören. Zum Schluss möchte ich meiner Familie danken, die mich während der ganzen Zeit unterstützt hat und auch mal für die richtige Ablenkung sorgte, wenn ich mal den Kopf frei kriegen musste.

Erklärung

Hiermit versichere ich an Eides statt, dass ich die vorliegende Dissertation mit dem Titel: "Advanced Time Imaging" selbstständig verfasst und keine anderen als die angegebenen Hilfsmittel – insbesondere keine im Quellenverzeichnis nicht benannten Internet-Quellen – benutzt habe. Alle Stellen, die wörtlich oder sinngemäß aus Veröffentlichungen entnommen wurden, sind als solche kenntlich gemacht. Ich versichere weiterhin, dass ich die Dissertation oder Teile davon vorher weder im In- noch im Ausland in einem anderen Prüfungsverfahren eingereicht habe und die eingereichte schriftliche Fassung der auf dem elektronischen Speichermedium entspricht.

Martina Glöckner